J. Fluid Mech. (2006), *vol.* 558, *pp.* 415–449. © 2006 Cambridge University Press
doi:10.1017/S0022112006000231 Printed in the United Kingdom

Contact angle dynamics in droplets impacting on flat surfaces with different wetting characteristics

By ILKER S. BAYER AND CONSTANTINE M. MEGARIDIS†

Department of Mechanical and Industrial Engineering, 842 W. Taylor Street,
University of Illinois at Chicago, Chicago, IL 60607, USA

(Received 24 January 2005 and in revised form 20 December 2005)

An experimental study is presented on contact angle dynamics during spreading/recoiling of mm-sized water droplets impacting orthogonally on various surfaces with $We = O(0.1) - O(10)$, $Ca = O(0.001) - O(0.01)$, $Re = O(100) - O(1000)$, $Oh = O(0.001)$ and $Bo = O(0.1)$. In this impact regime, inertial, viscous and capillary phenomena act in unison to influence contact angle dynamics. The wetting properties of the target surfaces range from wettable to non-wettable. The experiments feature accelerating and decelerating wetting lines, capillary surface waves in the early impact stages, contact angle hysteresis, and droplet rebound under non-wetting conditions. The objective of the work is to provide insight into the dynamic behaviour of the apparent (macroscopic) contact angle θ and its dependence on contact line velocity V_{CL} at various degrees of surface wetting. By correlating the temporal behaviours of θ and V_{CL}, the angle *vs.* speed relationship is established for each case examined. The results reveal that surface wettability has a critical influence on dynamic contact angle behaviour. The hydrodynamic wetting theory of Cox (*J. Fluid Mech.* vol. 357, 1998, p. 249) and the molecular-kinetic theory of wetting by Blake & Haynes (*J. Colloid Interface Sci.* vol. 30, 1969, p. 421) are implemented to extract values of the corresponding microscopic wetting parameters required to match the experimentally observed θ *vs.* V_{CL} data. Application of hydrodynamic theory indicates that in the slow stage of forced spreading the slip length and the microscopic contact angle should be contact line velocity dependent. The hydrodynamic theory performs well during kinematic (fast) spreading, in which solid/liquid interactions are weak. Application of the molecular kinetic theory yields physically reasonable molecular wetting parameters, which, however, vary with impact conditions. The results indicate that even for a single liquid there is no universal expression to relate contact angle with contact line speed. Finally, analysis of the spreading dynamics on the non-wettable surfaces shows that it conforms to the Cassie-Baxter regime (only partial liquid/solid contact is maintained). The present results offer guidance for numerical or analytical studies, which require careful attention to the implementation of boundary conditions at the moving contact line, including the need to specify the dependence of contact angle on contact line speed.

1. Introduction

Spontaneous (self) spreading of liquids over solid surfaces is of critical importance to several industrial technologies handling composites, adhesives, coatings and printing

† Author to whom correspondence should be addressed: cmm@uic.edu

https://doi.org/10.1017/S0022112006000231 Published online by Cambridge University Press

inks, as well as in agricultural plant treatment and oil recovery. As a consequence, spreading phenomena have been studied extensively (see for example deGennes 1985; Kistler 1993). Various aspects of the problem of wetting of solid surfaces by liquids have been investigated in the handling and storage of liquids in spacecraft under zero gravity conditions (Ellison & Tejada 1970; Schwartz & Tejada 1970, 1972). Spontaneous droplet spreading is generally driven by surface forces and is retarded by viscous forces. To date, most detailed experimental studies of the hydrodynamics of spontaneous droplet spreading have focused on cases where viscous forces are small compared to capillary forces, i.e. capillary number $Ca = \mu V_{CL}/\sigma \ll 1$, and inertia is negligible, i.e. Reynolds number $Re = D_0 V_0 \rho/\mu \ll 1$. In these dimensionless numbers, D_0 is the initial droplet diameter, V_0 the impact velocity, V_{CL} the contact line velocity, μ the liquid viscosity, σ the liquid surface tension, and ρ the liquid density.

In *forced* wetting, on the other hand, externally imposed hydrodynamic or mechanical forces introduce additional complexities during the rapidly progressing early stages of fluid spreading. For instance, droplet impact on a surface is dominated by inertia. The fluid dynamics of liquid films forced to spread over a solid surface is of enormous significance to engineering sciences, and in practice it is relevant to a host of emerging technologies. In free-form manufacturing (Orme, Huang & Courter 1996) for example, droplets of materials can be repeatedly dispensed in their molten form and subsequently solidify upon impact, producing a desired shape or structure. Objects, materials or components may be built up by precise deposition of molten micro drops under controlled thermal conditions. This provides a means of 'digital microfabrication,' or fabrication of three-dimensional objects micro drop by micro drop under complete computer control much in the same way as ink-jet printing (Gao & Sonin 1994). Another constructive application for metallic droplets is a technology known as solder jetting (Hayes *et al.* 1993). In this procedure, molten solder droplets with diameters between 50 and 100 μm are jetted on-demand onto specific landing pads located on a chip or other electronic substrate. Because of the fine temporal and spatial scales in solder jetting, experimental investigation of the relevant impact dynamics is challenging (Attinger, Zhao & Poulikakos 2000).

There exists a large volume of literature describing numerical modelling of droplet impact on solid surfaces (see Pasandideh-Fard, Chandra & Mostaghimi 2002 and references cited therein). Early numerical modelling studies in this area did not consider wettability effects, see for example Hatta, Fujimoto & Takuda (1995). Realistic simulations, which agree well with experiments, require careful attention to the implementation of boundary conditions, including the need to specify the dependence of contact angle on contact line speed (Fukai *et al.* 1995). As summarized by Davis (1983), mathematical modelling of wetting in the framework of conventional fluid mechanics has to circumvent fundamental difficulties due to the non-integrable shear-stress singularity at the moving contact line, and the inability to describe the velocity dependence of the dynamic contact angle (see review by Dussan 1979). Contact angle behaviour is intimately related to impact spreading dynamics, which is characterized primarily by the Weber and Ohnesorge numbers, respectively given by $We = \rho V_0^2 D_0/\sigma$ and $Oh = \mu/(\rho\sigma D_0)^{1/2}$. At high *We*, the droplet is driven radially outward by the impact-induced dynamic pressure gradient; at low *We*, the fluid is pulled out by the capillarity force at the contact line. The Ohnesorge number scales viscous resistance to spreading under the action of surface tension forces.

The objective of the present work is to provide insight into the dynamic behaviour of the apparent contact angle θ and its dependence on contact line velocity V_{CL} at various degrees of surface wetting for water droplets impacting axisymmetrically on

https://doi.org/10.1017/S0022112006000231 Published online by Cambridge University Press

substrates at low to moderate Weber numbers. Such data is required in numerical simulation of droplet impact. First, a synopsis is given on some prevalent dynamic wetting theories of hydrodynamic and molecular origin; these theories are considered later in the paper when processing and interpreting the experimental data. Maximum droplet spreading correlations are also tested against the current experimental data. Finally, special attention is given to droplet rebound on super-hydrophobic surfaces and the wetting mode applicable to these impact events.

2. Dynamic wetting theories

During droplet impact spreading, the contact line decelerates abruptly immediately after impact. This early rapid spreading defines the so-called kinematic spreading phase (Rioboo, Marengo & Tropea 2002), which is governed by the kinetic energy of the droplet. As the spreading progresses, wetting effects and liquid–solid interactions become important. The physics of the contact angle/contact line dynamics is unresolved under impact spreading conditions. We are interested in contact line dynamics under orthogonal impact conditions in which the Weber numbers remain below the threshold where three-dimensional features (like rivulets) start appearing. Since a main goal of the present study is to investigate the implementation of both hydrodynamic and molecular-kinetic theories of wetting in relating the contact angle variation with contact line velocity, the hydrodynamic theory of Cox (1986, 1998) and the molecular kinetic theory of Blake & Haynes (1969) are outlined first for completeness.

2.1. *Hydrodynamic theory*

When the flow field is calculated in the neighbourhood of a moving contact line, it is found that for all contact angles other than 180°, there is a non-integrable stress singularity at the contact line, resulting in a divergent integral drag force on the solid boundary (Huh & Scriven 1971; Dussan & Davis 1974). The stress diverges as $1/r$ when $r \to 0$, where r denotes the distance from the contact line. In order to avoid the singularity at $r = 0$, slip has been postulated to occur between the liquid and the solid surface at small distances, L_S, from the contact line (see Cox 1998 and references therein). Briefly, four types of slip conditions have been implemented by various researchers (Kistler 1993).

(i) Zero tangential stress at the solid surface at distances below L_S from the contact line and no slip for distances greater than L_S.

(ii) Difference in tangential velocity between liquid and solid (slip velocity) proportional to the local shear velocity gradient at the solid surface.

(iii) Slip velocity algebraically dependent upon distance from the contact line.

(iv) Slip velocity proportional to the p $(p > 0)$ power of the local shear velocity gradient.

Cox (1986) considered contact line movement for a general geometry in which one fluid displaces a second fluid, and for the special situation in which the flow is entirely viscous, $Re \ll 1$, (and therefore satisfies the Stokes equation). The main assumptions of Cox's viscous theory are that the contact line motion is steady, the liquid is advancing and the surface is ideally smooth. The flow field and the interface shape were found by Cox making a singular perturbation expansion in the capillary number. To perform the perturbation expansion, the conditions $Ca \ll 1$ and $L_S/L_H \ll 1$ were imposed, where L_H is a hydrodynamic macroscopic length scale. The macroscopic contact angle was defined by Cox in terms of the asymptotic angle that the interface

https://doi.org/10.1017/S0022112006000231 Published online by Cambridge University Press

makes with the solid surface as the contact line is approached at the macroscopic (experimental) lengthscale. Using the interface shape close to the contact line, Cox deduced an expression for the macroscopic contact angle in terms of the contact line speed V_{CL} and the microscopic contact angle θ_w. The latter was defined as the angle the liquid interface forms with the solid surface at distances of the order of the slip length L_S from the contact line.

For viscous contact line motion, the relationship between the capillary number and the macroscopic contact angle is given by

$$Ca = \frac{g_v(\theta) - g_v(\theta_w)}{\ln(L_H/L_S)} + O\left(\frac{1}{\ln(L_H/L_S)}\right)^2, \tag{2.1}$$

where the function $g_v(\theta)$ is given by

$$g_v(\theta) = \int_0^\theta \frac{\phi - \sin\phi\cos\phi}{2\sin\phi}\,\mathrm{d}\phi. \tag{2.2}$$

Equation (2.1) has found widespread use in modelling dynamic contact angles for liquid spreading (see Kistler 1993, for example). Attempts have also been made to combine this theory with the molecular kinetic theory of wetting (Petrov & Petrov 1992).

Cox (1998) extended his original theory to accommodate inertia-dominated contact line motion. The additional assumptions introduced for high-Reynolds-number flow are that only tangential motion is considered, the boundary layer is laminar and no flow separation occurs near the contact line. Also within the inner region, where both the slip length (L_S) and the microscopic contact angle (θ_w) are defined, the flow is irrotational. Especially for the more general situation, in which $1 \ll Re \ll L_H/L_S$, the presence of an intermediate region was introduced by Cox to bridge the viscous inner region and the inviscid outer region. Although slip lengths associated with moderate Weber number droplet impact spreading are not known a *priori*, it is argued that such liquid spreading could be modelled using the theory presented by Cox (1998). With θ^* denoting the value of the contact angle in the so-called transition sub-region (at $r^* \approx rV_{CL}\rho/\mu$) where inertia and viscous effects are of the same order, it is

$$Ca\ln(Re) = g_{iv}(\theta) - g_{iv}(\theta^*), \tag{2.3}$$

where the function g_{iv} is given by

$$g_{iv}(\theta) = 1.53162(\theta - \sin\theta). \tag{2.4}$$

The microscopic contact angle θ_w and θ^* are related by

$$Ca\,\ln\left(\frac{L_H}{L_S Re}\right) = g_v(\theta^*) - g_v(\theta_w). \tag{2.5}$$

Once $g_{iv}(\theta^*)$ is evaluated using (2.3) to fit the experimental data, θ^* can be determined from (2.4), and a subsequent curve-fitting step is required to determine θ_w and L_S using (2.5). There is, as pointed out by Cox, some experimental evidence to suggest that for some systems at least, the microscopic contact angle is a constant, whose value depends only on the particular liquid and solid surface involved. However, for systems in which the microscopic contact angle could depend on the spreading velocity, owing perhaps to effects at the molecular scale, Cox's theory is still valid but with $\theta_w = f(V_{CL})$. Indeed, experimental results by Garoff and co-workers (see Ramé, Garoff & Willson 2005 and references cited therein) have shown that the

https://doi.org/10.1017/S0022112006000231 Published online by Cambridge University Press

microscopic contact angle is velocity-dependent for a solid surface dipping slowly into a viscous liquid. A number of studies based on forced spreading of polar liquids on partially wettable surfaces yielded physically unreasonable values of the fixed slip length (Hayes & Ralston 1993). Naturally, the slip length depends on the solid surface characteristics and the specific solid–liquid interactions. Thus, it is conceivable that if the correct expression $\theta_w = f(V_{CL})$ is not known, then the value of L_S determined from fitting experimental data using either (2.1) or (2.5) and the assumption $\theta_w = const.$ could turn out to be physically unacceptable.

Shikhmurzaev (1993) has suggested that the contact angle is not only velocity-dependent, but also sensitive to the entire flow field near the wetting line. This model can accommodate more complex features of impact spreading, such as rolling, occurring early, or wedge-shape spreading, occurring late, but is considerably more intricate mathematically. Consequently, the application of Shikhmurzaev's theory is not within the scope of the present study, but will be analysed separately in future work.

2.2. *Molecular-kinetic (M-K) theory*

The *molecular-kinetic* theory of wetting, as developed by Blake & Haynes (1969), uses the theory of absolute reaction rates and asserts that the essential contact line motion takes place by jumping of molecules along the solid surface from the liquid to the vapour side of the contact line. According to this theory, the macroscopic behaviour of the wetting line depends on the overall statistics of the individual molecular displacements, which occur within the three-phase zone where the fluid–fluid interface meets the solid surface. The molecular-kinetic theory postulates that the entire energy dissipation occurs at the moving contact line. The wetting line moves with velocity V_{CL}, and the liquid exhibits a dynamic advancing contact angle θ such that $\theta > \theta_E$, where θ_E is the equilibrium contact angle. According to this theory, the velocity of the contact line is determined by the frequency κ and length λ of the individual molecular displacements that occur along its length. In the simplest model, these displacements take place at the adsorption sites on the solid surface. The length of the molecular displacement λ is influenced by the size of the liquid molecules and depends strongly on the spacing of the successive adsorption sites on the target surface. For the liquid molecules moving forward, the frequency of molecular displacement is κ^+, and for those moving backwards, the frequency is κ^-. The contact line velocity is then given by $V_{CL} = (\kappa^+ - \kappa^-)\lambda = \kappa\lambda$, where κ is the net frequency of molecular displacement (jump frequency). For the contact line to move, work must be done to overcome the energy barriers to molecular displacement in the preferred direction. This work is done by the surface tension force, which is $\sigma(\cos\theta_E - \cos\theta)$, as expressed per unit length of the contact line. The work done by this force is entirely within the contact point zone and any dissipation outside of this zone is neglected in the model. Combining these ideas and using Frenkel–Eyring activated rate theory of transport in liquids, the following relationship between θ and V_{CL} was obtained by Blake & Haynes (1969)

$$V_{CL} = 2\kappa_w \lambda \sinh\left[\frac{\sigma}{2nkT}(\cos\theta_E - \cos\theta)\right], \tag{2.6}$$

where k, T denote, respectively, Boltzmann's constant and the absolute temperature. The quantity n is the number of adsorption sites per unit area on the surface and is related to λ by $\lambda \sim n^{-1/2}$. In addition, the equilibrium jump frequency κ_w is related to

https://doi.org/10.1017/S0022112006000231 Published online by Cambridge University Press

the effective molar activation energy of wetting ΔG_W by

$$\kappa_w = \frac{kT}{h}\exp\left(\frac{-\Delta G_W}{N_A kT}\right), \tag{2.7}$$

where N_A is Avogadro's number and h stands for Planck's constant. For viscous flow in simple liquids, ΔG_W is about 10 kJ mol^{-1}, as in Blake (1993). High or low values of ΔG_W imply, respectively, strong or weak dependence of the contact angle on contact line speed.

A limitation of (2.7) is that it lacks consideration for viscous losses at the contact line, although this property may have a strong influence on the dynamic contact angle. In reality, both solid/liquid interactions and viscous molecular interactions are likely to operate at the contact line during spreading and/or recoil over the solid surface. A better approximation to the real mechanism of dissipation at the contact line is to combine viscous and liquid/solid interactions by writing $\Delta G_W = \Delta G_S + \Delta G_V$, where ΔG_S is the contribution arising from the retarding influence of the solid surface, and ΔG_V is the contribution due to the retarding influence of the liquid interactions at the molecular level. Combining this definition with (2.7), the following equation is obtained

$$\kappa_w = \frac{kT}{h}\exp\left(\frac{-\Delta G_S - \Delta G_V}{N_A kT}\right). \tag{2.8}$$

On the basis of the theory of absolute reaction rates (Glasstone, Laidler & Eyring 1941), the excess Gibbs activation energy ΔG_V can be calculated from

$$\mu = \frac{h}{v}\exp\left(\frac{\Delta G_V}{N_A kT}\right), \tag{2.9}$$

where v is the specific volume of the droplet fluid. Furthermore, if we define the solid/liquid interaction frequency as

$$\kappa_s = \frac{kT}{h}\exp\left(\frac{-\Delta G_S}{N_A kT}\right), \tag{2.10}$$

and combine (2.8), (2.9) and (2.10), we obtain

$$\kappa_w = \kappa_s\left(\frac{h}{\mu v}\right). \tag{2.11}$$

Hence, (2.6) can be rewritten as

$$V_{CL} = \frac{2\kappa_s h\lambda}{\mu v}\sinh\left[\frac{\sigma}{2nkT}(\cos\theta_E - \cos\theta)\right]. \tag{2.12}$$

An immediate demonstration of applying this theory is presented in table 1. Use of (2.12) with nonlinear least-squares-fit analysis of the experimental data of Schwartz & Tejada (1970, 1972) and subsequent use of (2.7)–(2.11) allows the extraction of the relevant molecular-kinetic parameters given in table 1. According to the theory outlined above, if liquid molecular interactions are weak, i.e. ΔG_V is negligible, then $\kappa_w \approx \kappa_s$. If solid/liquid interactions are also weak, i.e. κ_s is large, then (2.12) predicts θ to be weakly dependent on V_{CL}. Small equilibrium contact angles θ_E on a given surface mean strong solid/liquid interactions, whereas large equilibrium contact angles mean weak solid/liquid interactions. Inspection of the data in table 1 reveals that $\kappa_w \neq \kappa_s$, thus indicating that viscous dissipation at the contact line owing to liquid molecular interaction is not low for the liquid/solid systems tested by

https://doi.org/10.1017/S0022112006000231 Published online by Cambridge University Press

Liquid	Solid	θ_E (deg.)	μ (10^{-3}Ns m^{-2})	σ_L (10^{-2} N m^{-1})	λ (nm)	κ_w (10^7 s^{-1})	κ_s (10^{10} s^{-1})	ΔG_W (kJ mol^{-1})	$\Delta G_S/\Delta G_V$
Dioctyl sebacate	Teflon	61	25	3.12	1.40	0.002	0.18	48.6	0.7
Hexadecane	Steel	4	3.30	2.78	1.20	0.9	2	36.68	0.6
Ethanol	Steel	5	1.20	2.28	1.00	10	6.2	30.70	0.6
Octane	Teflon	26	0.54	2.18	0.98	28.4	4	28.16	0.7
Hexane	Steel	3	0.33	1.84	2.10	30	32	28.25	0.4
Methylene iodide	Nylon	41	0.50	5.10	0.80	1.4	0.13	35.67	1.4

TABLE 1. Molecular-kinetic wetting parameters (λ, κ_s) obtained from fitting (2.12) to the data of Schwartz & Tejada (1970, 1972) for various solid/liquid systems. κ_w, ΔG_S and ΔG_W were calculated from (2.11), (2.10) and (2.7), respectively.

Impact diameter, D_0	1.3–2.8 mm
Impact velocity, V_0	0.1–1.3 m s^{-1}
Equlibrium contact angle, θ_E	20°–157°
$Re = D_0 V_0 \rho/\mu$	140–2100
$We = \rho V_0^2 D_0/\sigma$	0.1–120
$Ca = \mu V_{CL}/\sigma$	0.006–0.01
$Oh = \mu/(\rho\sigma D_0)^{1/2}$	0.002–0.003
$Fr = V_0^2/gD_0$	0.7–70
$Bo = \rho D_0^2 g/\sigma$	0.2–0.9

TABLE 2. Parameter values in the present impact experiments. Dynamic contact angle measurements were made only for $We < 40$ to maintain axisymmetric conditions. Higher-Weber-number impact experiments were carried out only to measure the maximum spreading diameter on each surface (see § 4.2).

Schwartz & Tejada (1970, 1972). In addition, the calculated ratios of free energy of liquid/solid interactions to free energy of viscous dissipation at the molecular level ($\Delta G_S/\Delta G_V$) in table 1 are of special significance. If $\Delta G_S/\Delta G_V \gg 1$, then the liquid is likely to interact strongly with the solid surface, as for example, in aqueous glycerol on glass. If, on the other hand, $\Delta G_S/\Delta G_V \ll 1$ then the solid/liquid interactions are comparatively weak, as for example, in silicon oils on glass. The values of $\Delta G_S/\Delta G_V$ given in table 1 indicate that under the conditions investigated by Schwartz & Tejada (1970, 1972) both liquid/liquid and liquid/solid interaction forces at the molecular level jointly retard liquid front advancement.

3. Experimental

Single deionized water drops of controlled size and velocity (see table 2) were produced and vertically impacted onto different horizontal dry surfaces corresponding to wetting, partially wetting and non-wetting configurations. A KDS200 model infusion pump (KD Scientific) was used to dispense on demand single 1.3–2.8 mm ($\pm$0.03 mm) diameter water droplets from a 1 ml capacity syringe. The experimental set-up is shown in figure 1.

Droplet diameters were measured using a length calibration procedure, which was based on the known characteristic dimension of a spherical object placed momentarily along the droplet flight path. Changing the vertical distance between the syringe tip and the substrate varied impact velocities, which were determined

https://doi.org/10.1017/S0022112006000231 Published online by Cambridge University Press

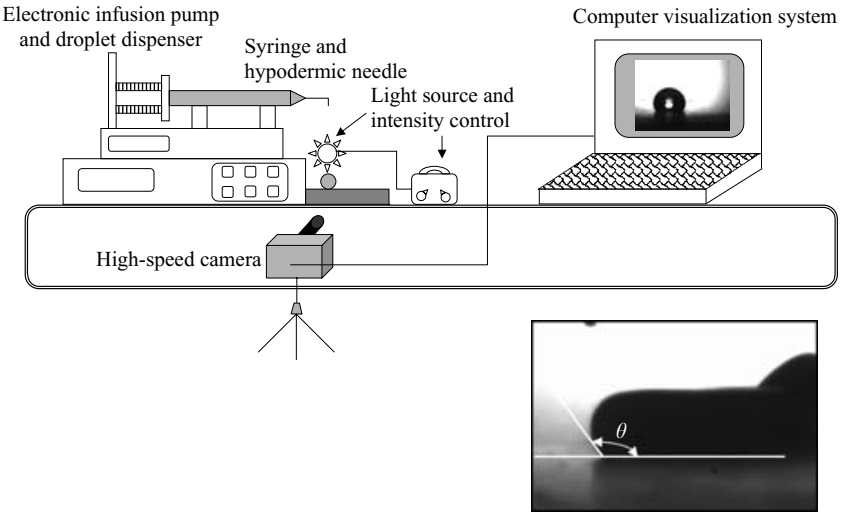


FIGURE 1. The experimental set-up. The inset shows an instantaneous image of a spreading droplet front. This image is typical of those captured with high-speed digital video for measuring the apparent dynamic contact angle θ.

using successive frames captured immediately before impact. An array of smooth substrates was used, spanning the range from wettable ($\theta_E < 40^\circ$) to non-wettable ($\theta_E > 140^\circ$). The typical wettable substrate was a mirror-polished stainless steel plate. The partially wettable surface was Surevent PVDF (polyvinylidene fluoride) membrane obtained from Millipore and the non-wettable surfaces were an ultra-hydrophobic polytetrafluoroethylene-coated silicon wafer and a fractal surface made from alkylketene dimer (AKD substrate) from Kao, Japan (see Shibuichi *et al.* 1998). Additional substrates included glass, Pyrex glass, polished aluminium and others, which are identified in this paper by the corresponding value of θ_E. High-speed digital motion pictures of single droplet impact and spreading were recorded at 3000–10000 frames s^{-1} with 1280×168 pixel resolution (at 3000 f.p.s.) using a Redlake Motion Pro image analyser at 30–54 ms exposure rate. The camera was fitted with an Optem Zoom 70 microscope lens (magnification range $0.75\times$ to $5.25\times$). A fibreoptic light source with variable intensity was used to backlight the droplet impact events. Measurements of droplet spread diameter and contact angle were made by a commercial image processing software. The inset in figure 1 depicts a sample frame showing a partial view of a droplet, whose contact line advances on a wettable smooth substrate. The horizontal white line marks the location of the solid surface, and the tangent line drawn indicates the dynamic contact angle θ. Experimentally, the apparent (macroscopic) contact angle is dependent on the magnification an optical microscope can yield. For the present work, the maximum magnification obtainable corresponded to 6.7 μm/pixel. This spatial resolution is considered satisfactory and falls below the characteristic length scale for fluid transport $(\mu D_0/\rho V_0)^{1/2} = O(10\,\mu\text{m})$, corresponding to the conditions in table 2. The wettable and partially wettable surfaces were cleaned with acetone and distilled water, and dried by compressed inert gas before use. Contact angle measurements were made from captured images with a resolution estimated to be $\pm 3^\circ$ at low speeds and up to twice that at higher impact speeds. Under fixed operating conditions, droplet sizes and velocities were reproducible within ± 0.03 mm and ± 0.03 m s^{-1}, respectively. Droplet height measurements (used

https://doi.org/10.1017/S0022112006000231 Published online by Cambridge University Press

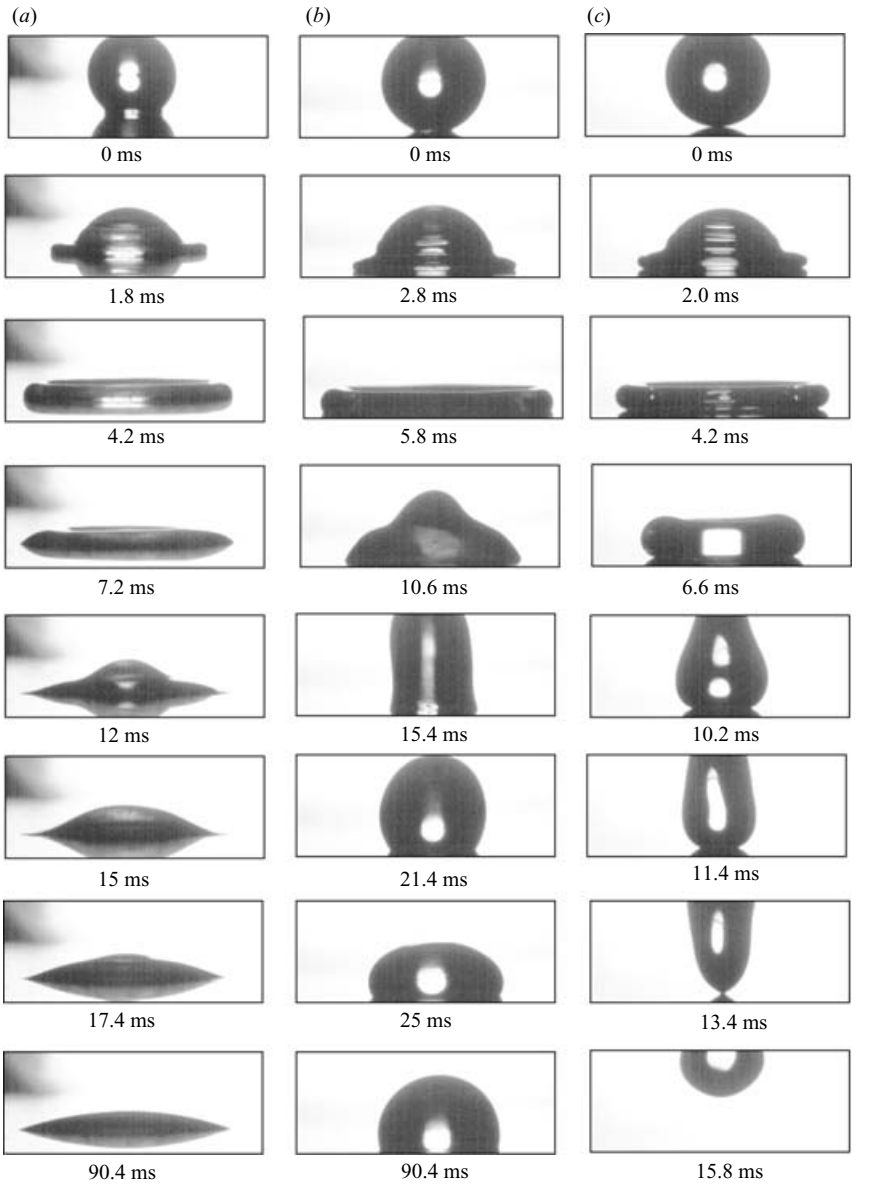


FIGURE 2. Impact of 1.4 mm diameter water droplets with $V_0 \sim 0.7\,\mathrm{m\,s^{-1}}$ on three flat surfaces with different degrees of wetting; (*a*) wettable, $We = 9.6$, (*b*) partially wettable, $We = 10$, and (*c*) non-wettable, $We = 9.3$. Because of its larger lateral spread on the wettable substrate, sequence (*a*) was recorded with a lower magnification than the sequences in (*b*) and (*c*), thus making the initial droplet diameter in (*a*) appear smaller than the other two.

for repeatability tests) were performed on images captured at a frame rate of 1000 f.p.s. with 512×512 pixel resolution, whereas at 3000 f.p.s., for example, the pixel resolution was 1280×168 allowing only vertically partial droplet view (see figure 2). To establish repeatability of the measurements, a single impaction event was repeated up to four times at first and the recordings were qualitatively compared to confirm the identical nature of the process. Then, the data from at least two identical experiments were

https://doi.org/10.1017/S0022112006000231 Published online by Cambridge University Press

analysed. The cross-experiment deviation in the measured droplet dimensions (spread diameter, height) was only $3-4\%$. In addition, the dynamic impact shapes were highly axisymmetric with the deviation between left and right dynamic contact angles remaining within $\pm 3^{\circ}$. This was attributed to the fact that surface morphology of the substrates was uniform and great care was exercised during surface cleaning. Given the high repeatability of these impact events, most of the results presented in the following sections pertain to single experiments.

4. Results and discussion

The parametric regime of this study (table 2) corresponds to impact conditions where no droplet splashing or fingering instabilities take place. Each droplet impact event produced an image sequence. The example shown in figure 2 displays three separate sequences, each recorded at 5000 frames s^{-1}. The backlit droplets appear dark against a bright background. The 'mirroring' of the droplet on the polished substrate below can be seen in all images. The sequence in figure 2(a) corresponds to impact on a wettable surface; figure 2(b) corresponds to impact on a partially wettable surface, and figure 2(c) to impact on a non-wettable surface.

4.1. *Capillary waves*

The severe free-surface deformation seen in the early impact stages of all sequences in figure 2 is accompanied by the formation of horizontal ripples (capillary waves) on the liquid/gas interface. Formation of such pyramidal structures was observed by Elliott & Ford (1972) for large water droplets impacting on partially wettable surfaces. Renardy *et al.* (2003) conducted experimental and numerical analysis of large water droplets ($D_0 = 3.5$ mm) impacting on non-wettable surfaces and observed that the droplets during the initial stages of spreading ($t < 5$ ms) deform into pyramidal structures with surface capillary waves propagating from the solid wall to the top of the drop. The present experimental observations indicated that such free-surface capillary waves become more pronounced as surface wettability decreases (left to right in figure 2). The analysis of Renardy *et al.* (2003) showed that there exists an impact velocity range in which surface capillary waves form during the early stages of spreading. This velocity range is given by

$$\left(\frac{2\sigma}{\rho D_0}\right)^{1/2} < V_0 < \left(\frac{2\sigma^2}{\rho\mu D_0}\right)^{1/3}, \tag{4.1}$$

a condition that was derived from the physical requirements $CaWe < 1$ and $We > 1$. The impact velocities in the present study fall largely in this regime, thus favouring capillary wave formation. Renardy *et al.* (2003) reported that the capillary wave of maximal amplification has a phase speed equal to the droplet impact speed, hence, the corresponding wavelength is $\Lambda = \sigma/(\rho V_0^2)$. Figure 3 shows an image sequence corresponding to a water droplet impacting on a non-wettable surface with $D_0 = 1.9$ mm and $V_0 = 0.33$ m s^{-1} ($We = 2.8$). The images are from the early stages of spreading when capillary waves are still visibly pronounced. These images allow measurement of wavelength and location of the capillary waves around the droplet periphery. As an example, figure 4(a) shows a single frame at 2 ms after impact with conditions similar to those of figure 3; four distinct capillary waves are visible on the droplet free surface. Nine capillary wavelengths are identifiable (marked $\Lambda_1, \Lambda_2, \ldots, \Lambda_9$), four on each side of the pyramid-shaped droplet, and one (Λ_5) on top. An ideal experiment would result in the formation of symmetric waves on both

https://doi.org/10.1017/S0022112006000231 Published online by Cambridge University Press

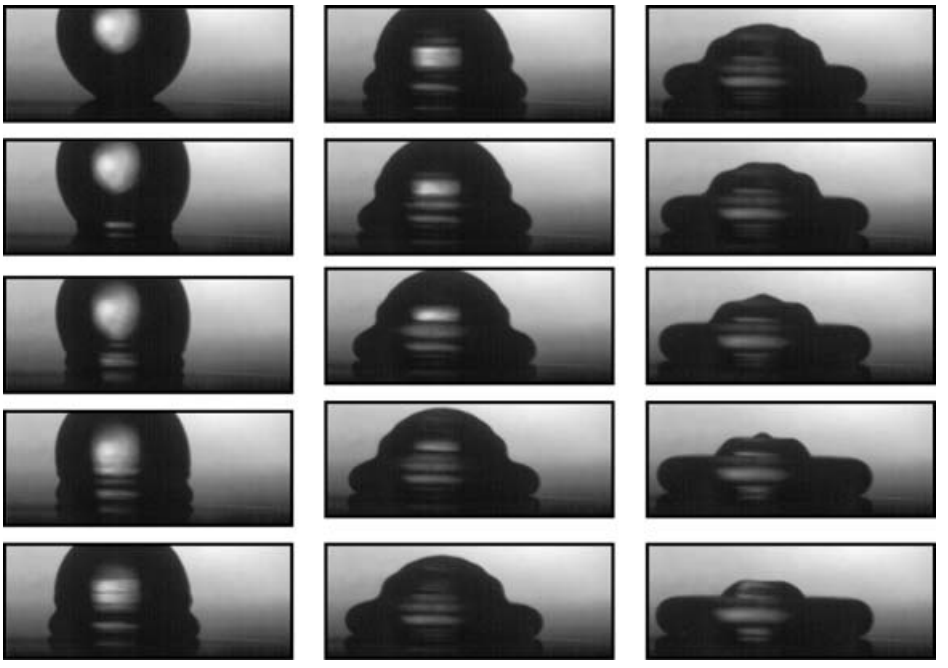


FIGURE 3. Early spreading showing formation of surface capillary waves on a water droplet impacting on a non-wettable surface with $D_0 = 1.9$ mm and $V_0 = 0.33\,\mathrm{m\,s^{-1}}$ ($We = 2.8$). Time proceeds from top to bottom and left to right. Successive frames are separated by 0.2 ms.

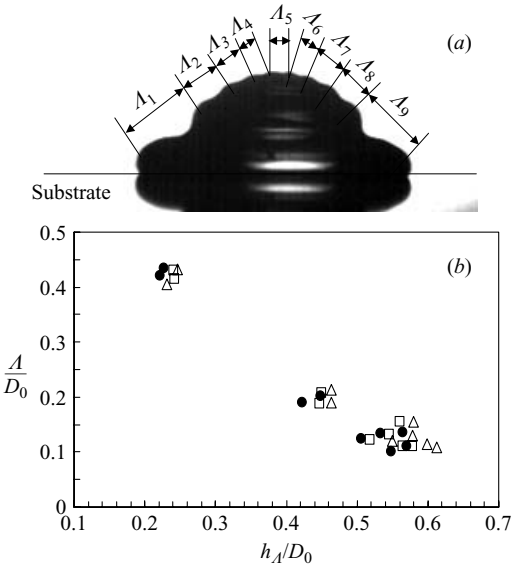


FIGURE 4. (*a*) Location and structure of capillary waves formed on the free surface of a droplet 2 ms after impact with $We = 3.3$, $Re = 585$. (*b*) Measured dimensionless wavelength of the capillary waves plotted as a function of normalized vertical distance from the substrate wall. Different symbols correspond to different conditions: ●, $\theta_E = 73°$, $We = 2.8$; □, $\theta_E = 93°$, $We = 3.2$, △, $\theta_E = 140°$, $We = 3.4$.

https://doi.org/10.1017/S0022112006000231 Published online by Cambridge University Press

Impact *We*	*WeCa*	Λ_{exp} (mm)	$\Lambda = \sigma/(\rho V_0^2)$ (mm)
3.5	0.367	0.33	0.23
2.1	0.187	0.36	0.32
3.4	0.185	0.28	0.22
2.9	0.140	0.36	0.32
4.3	0.124	0.29	0.23
1.8	0.05	0.50	0.56

TABLE 3. Capillary wavelengths Λ_{exp} measured from six different experiments with $We \approx 3$. Initial droplet diameters ranged from 1.4 to 2.8 mm, while impact velocities ranged from 0.4 to 1.3 m s^{-1}. The values of Λ_{exp} were those in figure 4(*b*) corresponding to $h_\Lambda/D_0 = 0.4 - 0.5$.

sides of the pyramid. The graph in figure 4(*b*) is for several impacts with $We \approx 3$ and plots the values of normalized wavelengths versus normalized distance from the wall (h_Λ/D_0) for droplet shapes recorded at 2 ms. Six different experiments – two at each condition – were considered for this plot. It can be seen that maximum values of Λ occur close to the wall (low h_Λ), and vice versa. In order to perform comparisons with the analysis of Renardy *et al.* (2003), table 3 gives experimentally observed capillary wavelength data at a mid-distance from the wall ($h_\Lambda/D_0 \approx 0.4-0.5$), along with values of the theoretical maximum amplification wavelength $\Lambda = \sigma/(\rho V_0^2)$. The agreement is favourable, thus supporting the physical arguments put forth by Renardy *et al.* (2003).

After the formation of the capillary waves upon initial impact in figure 2, flattening of the droplet follows ($t \approx 4$ ms) with subsequent recoil on the partially wettable surface (figure 2*b*) and droplet rebound on the non-wettable surface ($t = 13.4$ ms in figure 2*c*). It is emphasized that under these impact conditions, rebound occurred on neither the wettable nor the partially wettable substrates.

The entire discussion in this paper pertains to events after the very early impact stage, during which the contact angle is expected to decrease from 180° (in an ideal case, where the droplet is a perfect sphere upon impact) to lower values. In almost all recorded impact sequences, the first image showing contact of droplet/substrate did not coincide with the instant when $\theta = 180°$. Consequently, all reported temporal curves for θ start at values $\theta < 180°$. In addition, at high impact speeds, the contact line moved too fast to be visualized clearly, even at the high recording rates used. Therefore, contact angle measurements were made only when the interface definition around the contact line was clear.

4.2. *Spreading characteristics*

The instantaneous values of lateral droplet spread D_m (normalized with respect to D_0) are plotted in figure 5 with respect to time. D_m typically corresponded to droplet locations off the substrate; therefore, this parameter was not equivalent to the contact line diameter, which was measured separately and subsequently differentiated to produce contact line speed (V_{CL}) data. The three curves in each of the two graphs in figure 5 represent impacts with the same diameter ($D_0 = 1.4$ mm) and velocity (figure 5*a*, 0.77 m s^{-1}, figure 5*b*, 0.45 m s^{-1}) on wettable, partially wettable and non-wettable substrates. While contact line retraction is clear in non-wetting or partially wetting curves, for the wettable surface only slight droplet retraction is observed for $V_0 = 0.77$ m s^{-1}. In the early spreading portion of the curves shown in figure 5, the ratio D_m/D_0 increases approximately as $t^{0.5}$ until it reaches its peak value. This

https://doi.org/10.1017/S0022112006000231 Published online by Cambridge University Press

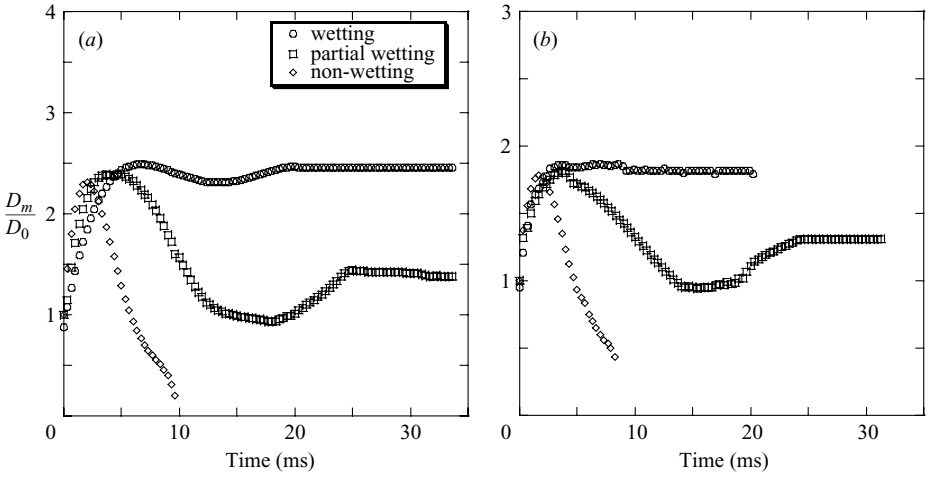


FIGURE 5. Maximum lateral spread ratio of 1.4 mm diameter water droplets impacting on surfaces with different wetting characteristics. Effect of impact velocity: (*a*) $V_0 = 0.77\,\mathrm{m\,s^{-1}}$ ($We = 11.5$), (*b*) $V_0 = 0.45\,\mathrm{m\,s^{-1}}$ ($We = 3.9$). The three curves in (*a*) correspond to impacts very similar to those shown in figure 2.

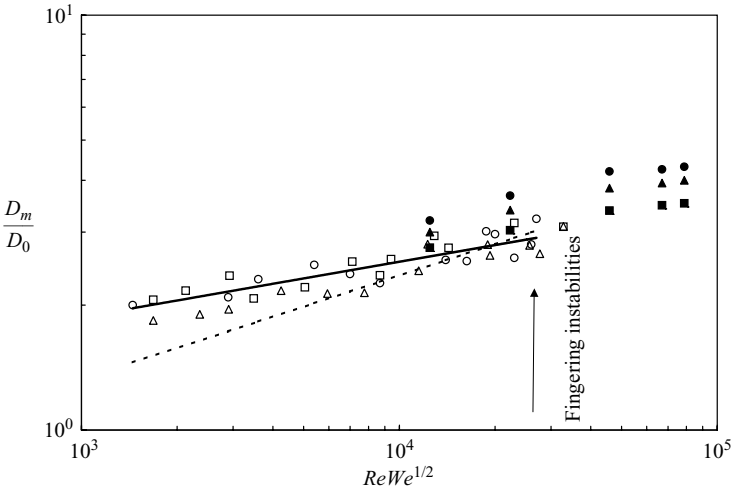


FIGURE 6. Influence of surface wettability on maximum droplet spreading. ○, $\theta_E = 20°$; □, $\theta_E = 74°$; △, $\theta_E = 135°$. Filled symbols display experimental data from Ford & Furmidge (1967); ●, $\theta_E = 27°$; ■, $\theta_E = 62°$; ▲, $\theta_E = 111°$. The solid line represents a regression fit to the present experimental data ($D_m/D_0 = 0.72\ (Re\,We^{1/2})^{0.14}$), whereas the dashed line depicts the correlation $D_m/D_0 = We^{1/4}$ by Clanet *et al.* (2004). To plot the latter, for each *We*, the corresponding *Re* was calculated from $Re = (\sigma\rho D_0 We)^{1/2}/\mu$. Both correlation lines are terminated at $ReWe^{1/2} = 2.7 \times 10^4$, where fingering instabilities are expected to appear.

temporal variation is consistent with the experimental results of Rioboo *et al.* (2002). In addition, the peak values of D_m/D_0 in figure 5 seem to be relatively insensitive to the wetting character of the solid surface. In order to further investigate the effect of surface wettability (θ_E) on maximum droplet spreading, a set of experiments was conducted with droplet impact velocities in the range 0.47–2.4 m s^{-1} ($3 < We < 120$). Figure 6 shows peak spreading diameters as a function of $Re\sqrt{We}$ for different

https://doi.org/10.1017/S0022112006000231 Published online by Cambridge University Press

substrates (wetting to non-wetting). Dimensional analysis gives four independent dimensionless groups to characterize drop impact (Schiaffino & Sonin 1997). The ratio of liquid–solid surface energies and gravity is not expected to be important at significant impact velocities. We chose $Re\sqrt{We} = Re^2Oh$ to characterize drop impact spreading dynamics because this combination involves both kinematic and material properties. Inspection of figure 6 reveals that measured D_m/D_0 ratios collapse into a single regression line given by

$$D_m/D_0 = 0.72\left(ReWe^{1/2}\right)^{0.14}. \tag{4.2}$$

This outcome supports the conclusion that maximum droplet spreading remains relatively insensitive to surface wettability, at least for the axisymmetric inertia-dominated impacts presented here. Figure 6 also includes the impact spreading data of Ford & Furmidge (1967) corresponding to surfaces with $27^\circ < \theta_E < 111^\circ$. Their impact experiments were performed at higher Weber numbers with the aim of simulating industrial spray droplet interactions. Although some of the data of Ford & Furmidge (1967) shown in figure 6 cross over to the regime where axisymmetry is expected to break down (i.e. fingering instabilities appear), they are included to show the overall trend. The maximal droplet spreading correlation ($D_m/D_0 \sim We^{1/4} \sim V_0^{1/2}$) put forth by Clanet *et al.* (2004) is also shown in figure 6 as a dashed line. This correlation seems to predict the present experimental data reasonably well, especially in the range $ReWe^{1/2} > 10^4$. However, the same correlation underestimates the present data at $ReWe^{1/2} < 10^4$. Similar spreading correlations reported earlier for viscous fluids are of the form $D_m/D_0 \sim Re^{1/5} \sim V_0^{1/5}$ (see figure 9 in Clanet *et al.* 2004). Clanet *et al.* (2004) neglected viscous dissipation in examining droplet deformation data on highly non-wettable surfaces with $10 < We < 900$. According to figure 6, the fitting correlation $D_m/D_0 \sim (ReWe^{1/2})^{0.14}$ gives $D_m/D_0 \sim V_0^{2/7}$, which indicates, for the present experimental data, a weaker dependency of spreading on impact velocity than that reported in Clanet *et al.* (2004). In the present study, a low-viscosity fluid (water) is used, but the surfaces have widely disparate wetting properties (wetting to non-wetting), which could be responsible for the observed discrepancy. Specifically, liquid–solid interactions seem to play a role in limiting droplet spreading under the present conditions. Earlier in the discussion related to table 1 and the data of Schwartz & Tejada(1970, 1972), it was shown that viscous dissipation and solid–liquid interactions play equally important roles in retarding contact line motion (see $\Delta G_S/\Delta G_V$ ratios in table 1). The condition $\Delta G_S/\Delta G_V \approx 1$ is also valid for the present experimental conditions, as will be shown in § 4.5 (see table 7). As a result, the difference between the present spreading correlation and that of Clanet *et al.* (2004) is attributed to liquid–solid interactions, which are expected to be more pronounced in the lower Weber number range applicable to the present work.

In figure 5, after spreading is completed, recoiling may follow, depending on surface wettability. In the case of the non-wettable substrate, recoiling terminates in complete rebound (see also figure 2*c*). On the partially wettable surface, the recoil is completed between 10 and 15 ms and is subsequently followed by a second spreading cycle (figure 5). However, on the wettable target, very little recoil occurs (see figure 5). The capillarity force arising from the difference between equilibrium droplet shape and deformed droplet shape drives the recoiling flow. The degree of droplet recoil is a strong function of the equilibrium contact angle, as shown in figure 7, which plots the normalized values of receding contact line speed versus dimensionless time for four droplets of identical pre-impact diameter and velocity, but each impacting on a surface of different wettability (wetting to non-wetting). Although, the maximum

https://doi.org/10.1017/S0022112006000231 Published online by Cambridge University Press

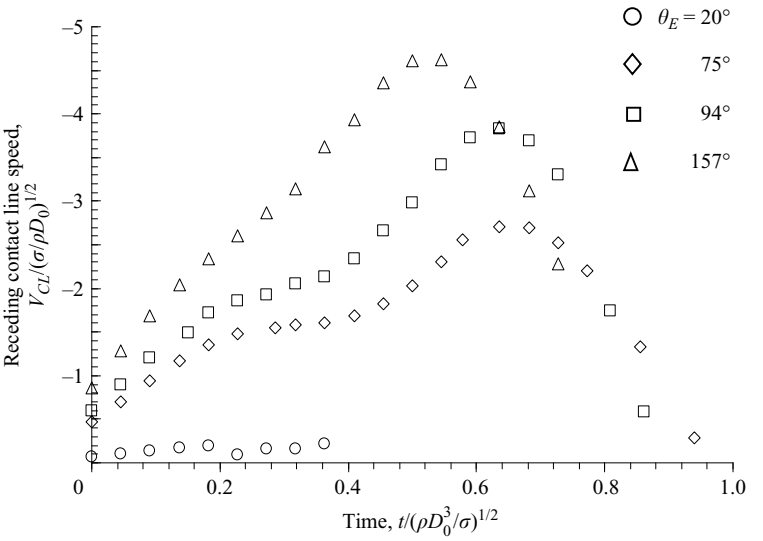


FIGURE 7. Effect of surface wettability on receding contact line speed. This speed is scaled by $(\sigma/\rho D_0)^{1/2}$, while time is scaled by $(\rho D_0^3/\sigma)^{1/2}$. Impact conditions: $D_0 = 1.65$ mm and $V_0 = 0.72\,\mathrm{m\,s^{-1}}$ ($We = 12$).

spreading diameters for these four impact cases are essentially alike, the recoiling rate is moderated by increased wetting (compare data for $\theta_E = 157°$ with $\theta_E = 94°$, 75° and 20° in figure 7). Physically, this trend can be understood by considering the equilibrium spreading of a droplet on a wettable and a non-wettable surface. The equilibrated droplet on the non-wettable surface does not extend laterally as much as on a wettable surface. Therefore, when the droplet spreads wider than its equilibrium state under the effect of impact inertia, the liquid on the non-wettable surface has a stronger tendency (i.e. higher recoil velocity) to reduce its contact area compared to the droplet striking the wettable surface. Inspection of figure 7 indicates that for equilibrium contact angles $75° < \theta_E < 160°$, the receding contact line is initially accelerated, reaching a zero acceleration plateau and then decelerates steadily to the end of retraction.

As seen in figure 5, the recoil rate on the non-wettable surface is very similar to the spreading rate, thus indicating minimal interaction between the liquid and the solid substrate. It is also noted that the residence times (contact period of the droplet from initial impact to rebound) are very similar for the two non-wetting impacts in figure 5, in agreement with the results of Bergeron *et al.* (2000). Okumura *et al.* (2003) studied bouncing drops and used a model supported by experimental data to show that residence times of a liquid drop impacting with $V_0 > 0.4\,\mathrm{m\,s^{-1}}$ on a non-wettable surface are insensitive to impact inertia. The present results support this finding, as can be seen by the non-wetting curves in figure 5. By adding trace amounts of a flexible polymer to water, Bergeron *et al.* (2000) were able to prevent droplet rebound. They found that by the polymer addition, the elongation viscosity of the liquid was increased dramatically, thus dampening drop retraction, and eventually preventing rebound. They reported that droplets with receding velocity less than $0.3\,\mathrm{m\,s^{-1}}$ did not bounce. In the present study, for the non-wettable substrate with $V_0 = 0.77\,\mathrm{m\,s^{-1}}$ (figure 5*a*), the average receding velocity was calculated to be $0.51\,\mathrm{m\,s^{-1}}$, whereas for $V_0 = 0.45\,\mathrm{m\,s^{-1}}$ (figure 5*b*), the receding velocity was $0.34\,\mathrm{m\,s^{-1}}$. In both

https://doi.org/10.1017/S0022112006000231 Published online by Cambridge University Press

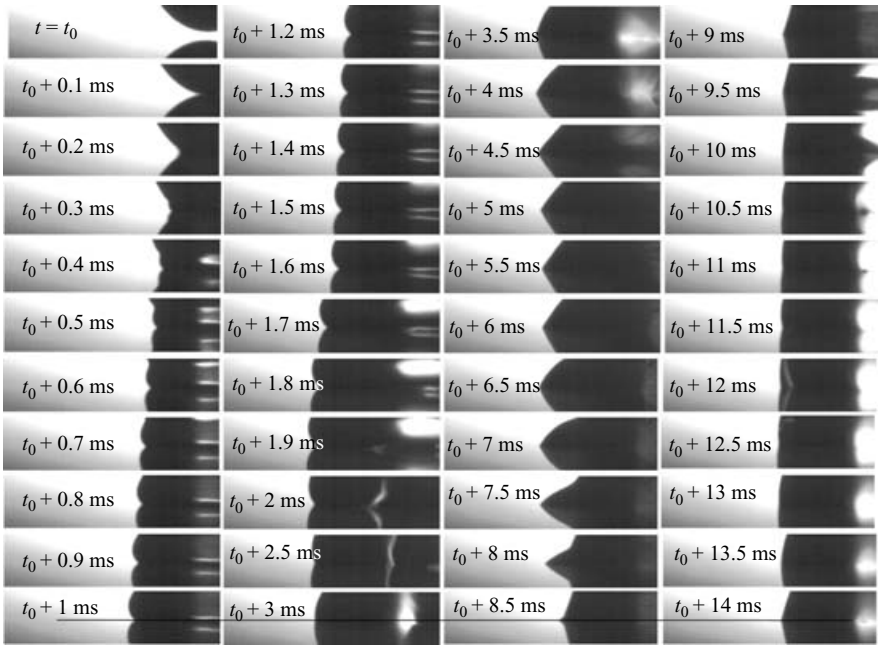


FIGURE 8. Partial close-up view of a water droplet impinging on a partially wettable surface with $We = 6$. This sequence follows the motion of the advancing/receding contact line along with the changes in the apparent contact angle. The horizontal line in the bottom row marks the location of the substrate.

cases rebound was observed. On the partially wettable surface, however, the average receding velocity was found to be $0.25\,\mathrm{m\,s^{-1}}$ for $V_0 = 0.77\,\mathrm{m\,s^{-1}}$ and $0.12\,\mathrm{m\,s^{-1}}$ for $V_0 = 0.45\,\mathrm{m\,s^{-1}}$. No rebound was observed on the partially wettable surface (see figure 5), being consistent with the $0.3\,\mathrm{m\,s^{-1}}$ receding velocity threshold reported by Bergeron *et al.* (2000).

4.3. *Apparent contact angle dynamics*

Figure 8 shows a typical close-up droplet impact sequence recorded with 0.1 ms resolution for an advancing/receding front on a partially wettable surface. The 'tank tread' type contact line advancement is noticeable until 3 ms after initial contact; during this period the surface wettability effects are negligible. However, as receding starts, wettability and surface tension effects become important. The present data indicate that during the initial spreading, the contact line decelerates steadily up to contact line arrest. Subsequently, during the recoil (figure 7) the contact line initially accelerates and then decelerates before it comes to a second stop. Finally, a new spreading cycle is initiated, with the contact line accelerating and then decelerating before it arrests again. Of course, not all steps described above apply to non-wetting impact, which can terminate (rebound) at the end of the first recoil (figure 2). Such experiments – featuring both accelerating and decelerating wetting lines – offer an attractive platform to resolve contact angle dependence on contact line speed (or its temporal rate of change).

Figure 9 shows the results of a series of experiments conducted to investigate the effect of impact inertia on contact angle dynamics for two different surfaces; one wettable ($\theta_E = 36°$), and another partially wettable ($\theta_E = 85°$). All droplets in this

https://doi.org/10.1017/S0022112006000231 Published online by Cambridge University Press

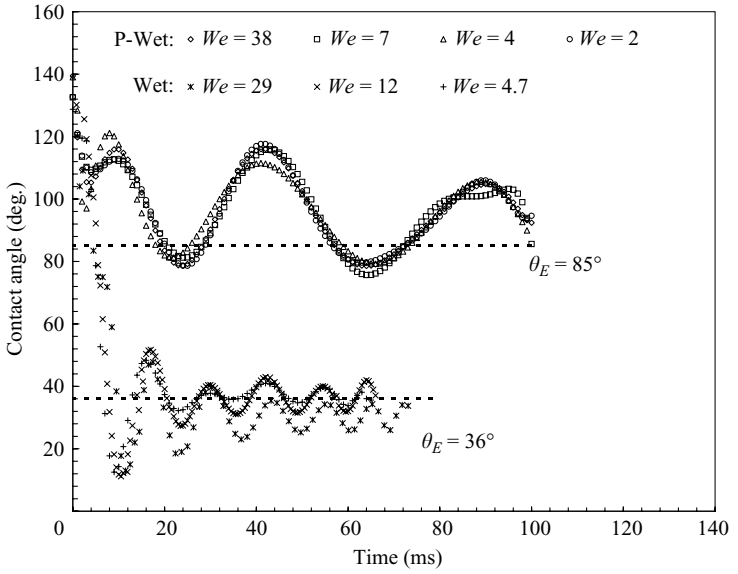


FIGURE 9. Time history of apparent dynamic contact angle of ~ 1.9 mm water droplets impacting with variable velocity ($0.28 - 1.2\,\mathrm{m\,s^{-1}}$) on a partially wettable (P-Wet, $\theta_E = 85°$) and a wettable surface (Wet, $\theta_E = 36°$). The values of Weber number for each impact are given in the key.

figure had diameters in the narrow range 1.7—2.1 mm, and impacted with velocities from $0.28\,\mathrm{m\,s^{-1}}$ to $1.2\,\mathrm{m\,s^{-1}}$, corresponding to *We* in the range 2—38. During the very early period (< 10 ms) in figure 9, the initially spherical droplets adjust to the impenetrable flat wall, with the contact angles dropping precipitously to levels approaching their equilibrium values. The values of θ oscillates around this level thereafter, thus indicating that surface wettability has a critical influence on dynamic contact angle values. For the partially wettable surface (top curves in figure 9), oscillations in θ display almost the same amplitude and frequency, also remaining in phase. This finding suggests that impact inertia has practically no influence on contact angle dynamics in this regime. For the wettable surface (bottom curves in figure 9), contact angle oscillations occur with the same frequency and are also in phase. However, as impact inertia increases, the contact angle curves reach lower levels, apparently due to the extended lateral stretch of the liquid on the wettable surface, which, by not allowing recoil, forces contact angles below levels attained at reduced Weber numbers. Nonetheless, for impact on wettable surfaces the effect of inertia on contact angle dynamics appears to be limited in this range $We = 2 - 40$. On the other hand, the results of figure 9 reveal that surface wettability has a critical influence on contact angle dynamic behaviour, with increased wettability resulting in higher frequency and lower oscillation magnitude. It is of interest to compare the contact angle oscillation frequencies seen in figure 9 with the natural oscillation frequency of a liquid droplet surrounded by a gas medium, namely, $f_N = [16\sigma/(\pi^2 \rho D_0^3)]^{1/2}$ (Clift, Grace & Weber 1978, pp. 187–188). For the average drop diameter $D_0 = 1.9$ mm applicable to figure 9, the natural oscillation frequency is $f_N = 130$ Hz, a value at the high end of the contact angle oscillation frequencies seen in this figure, namely, 20–30 Hz on the partially wettable surface, and 75–110 Hz on the wettable surface.

https://doi.org/10.1017/S0022112006000231 Published online by Cambridge University Press

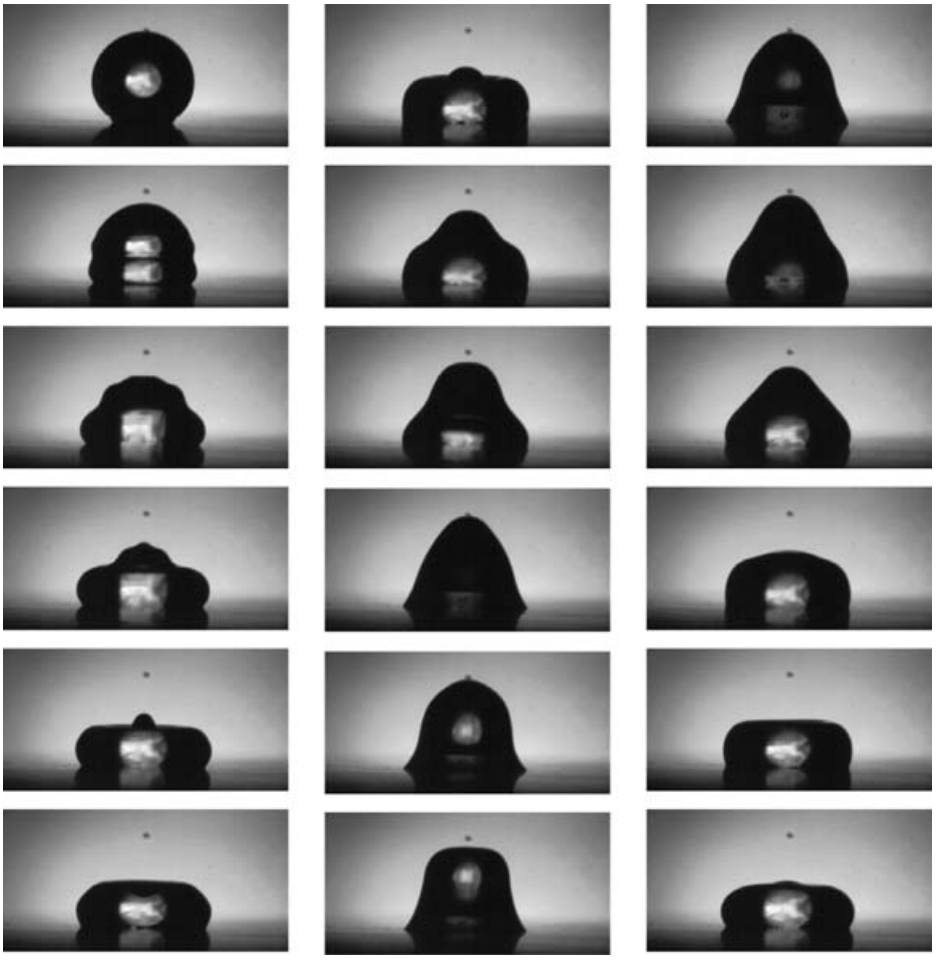


FIGURE 10. Low Weber number ($D_0 = 2.1$ mm, $V_0 = 0.16\,\mathrm{m\,s^{-1}}$, $We = 0.7$) droplet impact and post-spreading droplet oscillations on a silicon rubber surface with $\theta_E = 91°$. Time proceeds from top to bottom in each column at 0.5 ms intervals. The contact line is pinned at $t \sim 5$ ms from impact (half-way in the middle column). The background speck above the droplet is unrelated to the liquid.

Dynamic wettability of industrially relevant polymers such as Teflon, silicon rubber, polycarbonate and polyvinyl rubber has been studied for some time owing to the extensive use of these materials as insulators (Owen *et al.* 1988). Equilibrium contact angles for water on these materials is up to 90°. Contact angle dynamics on such surfaces is intimately connected with loss of hydrophobicity and surface structure changes, therefore, impact experiments on hydrophobic polymers provide insight into the practical performance of these materials. Post-spreading contact angle oscillations are very common when droplets impact on hydrophobic rubber surfaces with low Weber number. Figure 10 exemplifies such dynamics, where oscillations persist even after 200 ms (not shown).

As in figure 9 for $We > 1$, figure 11 examines the effect of impact inertia on contact angle dynamics for $We < 1$. A partially wettable ($\theta_E = 80°$) and a wettable ($\theta_E = 24°$)

https://doi.org/10.1017/S0022112006000231 Published online by Cambridge University Press

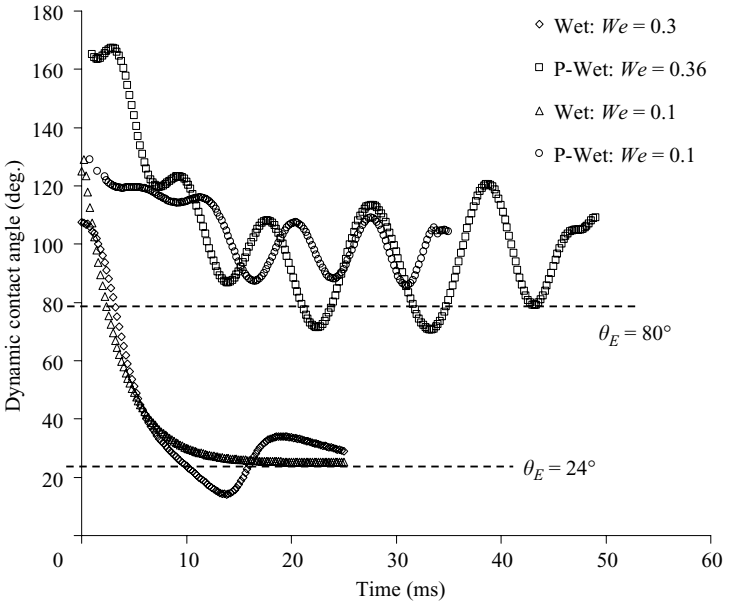


FIGURE 11. Time history of apparent dynamic contact angle of 1.5 mm water droplets impacting with variable velocity ($0.1 - 0.36\,\mathrm{m\,s^{-1}}$) on a partially wettable (P-Wet, $\theta_E = 80°$) and a wettable surface (Wet, $\theta_E = 24°$). The corresponding values of Weber number are given in the key.

surface were used in these experiments. The results confirm that surface wettability strongly affect contact angle dynamics. However, contrary to what was observed at moderate Weber numbers for partially wettable surfaces, impact inertia now affects both frequency and amplitude of contact line oscillations. This is probably due to the increased influence of surface tension at $We < 1$, which can now compete more effectively with inertia, especially locally in the region of the triple line. On the wettable surfaces, the contact angle declines precipitously in the early stages, irrespective of impact inertia. At $We = 0.1$, θ declines steadily towards its equilibrium value. However, when inertia increases (see $We = 0.3$ curve), oscillations appear and persist for a short period until θ reaches θ_E.

Figure 12 shows contact angle variations corresponding to a fixed droplet diameter $D_0 = 1.4$ mm and velocity (*a*) $V_0 = 0.77\,\mathrm{m\,s^{-1}}$, or (*b*) $V_0 = 0.45\,\mathrm{m\,s^{-1}}$. As seen, variations in surface wettability critically affect contact angle dynamics although the pre-impact conditions remain unchanged. It is noted that the droplet impact kinetic energy in figure 12(*a*) is three times higher than that in figure 12(*b*). At lower impact energy (figure 12*b*), receding on a wettable surface is barely noticeable (see also figure 5*b*) and the contact angle after 10 ms remains essentially fixed at $\sim 20°$. During the early stages of impact on the partially wettable surface, the contact angle remains between 130° and 140°. This period corresponds to a spreading stage where the contact line advances at a rate close to the impact velocity. After this period, the contact angle decreases rapidly until maximal spread is reached. During receding (between 5 and 13 ms in figure 5), the dynamic contact angle continues to decrease at a considerably lower rate until a minimum is attained. This observation is in agreement with the results of Elliott & Ford (1972) who examined partial wetting dynamics of various

https://doi.org/10.1017/S0022112006000231 Published online by Cambridge University Press

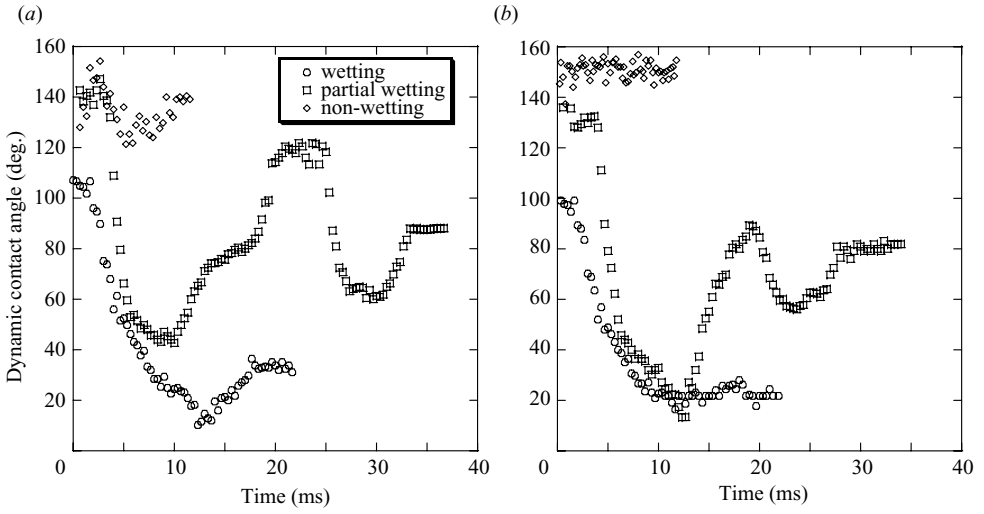


FIGURE 12. Time variation of apparent contact angle for 1.4 mm diameter water droplets impacting on surfaces with varying wetting characteristics. (*a*) $V_0 = 0.77\,\mathrm{m\,s^{-1}}$ ($We = 11.5$), (*b*) $V_0 = 0.45\,\mathrm{m\,s^{-1}}$ ($We = 3.9$).

droplets. Between 13 ms and 21 ms after impact, the droplet spread diameter stays practically constant (figure 5) and the bulk liquid is pushed toward the contact line, thus increasing θ (figure 12) before the droplet begins a new (second) spreading cycle. This second spreading stage lasts for about 5 ms, during which the apparent dynamic contact angle exceeds 90° and reaches a maximum. Before termination of the second spreading, the contact angle starts decreasing again, reaching a plateau before increasing slightly once again and stabilizing between 80° and 90° (figure 12). At this stage, apparent contact angle variations are due solely to bulk fluid oscillations above the contact line. The non-wetting spreading data in figure 12 show that the dynamic contact angles for the high- and low-impact velocity cases remain in a narrow range (121° − 155° and 143° − 157°, respectively) without any significant influence from the bulk fluid oscillations. Advancing/receding front shapes do not change ($\theta_A \sim \theta_R$), indicating that the wetting effects are negligible.

In figure 13, a magnified partial view of a water droplet at maximum spreading is displayed. The impact conditions are $D_0 = 2.1$ mm and $V_0 = 0.53\,\mathrm{m\,s^{-1}}$ ($We = 8$). The substrate is partially wettable and throughout this stage the contact line is pinned temporarily. The apparent contact angle decreases from $\theta_1 \sim 125°$ (top) to $\theta_4 \sim 40°$ (bottom) in about 5 ms. This phenomenon is known as dynamic contact angle hysteresis and has a profound effect on post-deposition droplet dynamics on a given surface.

4.4. *Application of the Cox hydrodynamic theory*

In this section, we apply the general Reynolds number theory of Cox (1998) to droplet impact spreading experiments with low to moderate Weber numbers in order to deduce values for the microscopic parameters describing contact line flow. In addition, the theory by Cox (1986) is implemented against the forced spreading data of Ellison & Tejada (1970) to further investigate the dependence of the microscopic flow parameters on the specific $\theta - V_{CL}$ behaviour on a given surface.

https://doi.org/10.1017/S0022112006000231 Published online by Cambridge University Press

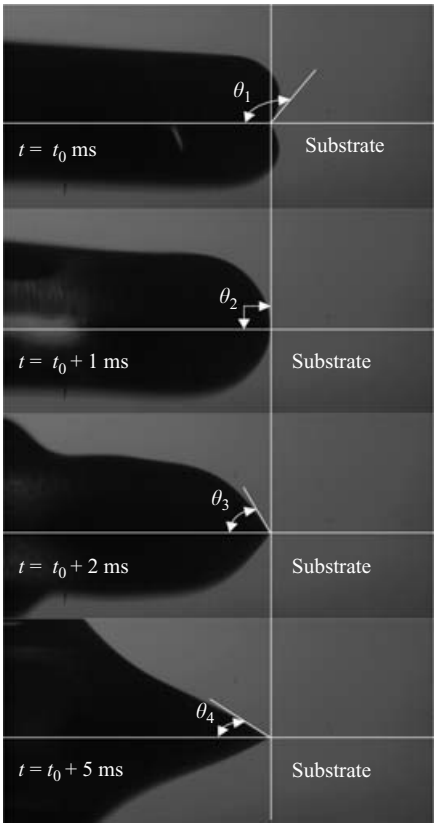


FIGURE 13. Partial view of a 2.1 mm diameter water droplet striking a partially wettable surface with $V_0 = 0.53\,\mathrm{m\,s^{-1}}$ ($We = 8$). This image sequence depicts how the apparent contact angle changes when the contact line is arrested temporarily after peak spreading. The vertical white line marks the position of the pinned contact point and the horizontal lines in each frame designate the surface, below which the droplet mirror image is seen ($\theta_1 = 125°$, $\theta_2 = 90°$, $\theta_3 = 62°$ and $\theta_4 = 40°$).

Figure 14 shows the contact angle variation with contact line speed for water droplets impacting on a partially wettable surface at low Weber numbers. The inset in figure 14 is a plot of $g_v(\theta^*)$ versus capillary number for the same data set. The slip length and the microscopic contact angle can be determined using the inset (see equations (2.3) to (2.5)). Two approaches are possible, i.e. implementing the Cox theory to the entire data set, as was done in the experiments of Hayes & Ralston (1993), or analysing the data below and above a critical Capillary number at which the sensitivity of the contact angle to contact line velocity changes. Even though the impact Weber numbers are low, the kinematic spreading regime is still present and a curve-fitting algorithm to the entire data set resulted in sub-molecular slip lengths. Therefore, the data were analysed for each Weber number by considering the kinematic and final spreading stages separately. The microscopic parameters extracted from the data of figure 14 are given in table 4. Slip lengths range from sub-molecular values to $O \sim (1\,\mathrm{nm})$. This outcome shows the sensitivity of the microscopic parameters to the impact conditions. Especially, slip lengths evaluated at the final stage of spreading ($V_{CL} < 0.2\,\mathrm{m\,s^{-1}}$) are physically unreasonable. This indicates that slip lengths describing droplet impact spreading are more likely to be dynamic

https://doi.org/10.1017/S0022112006000231 Published online by Cambridge University Press

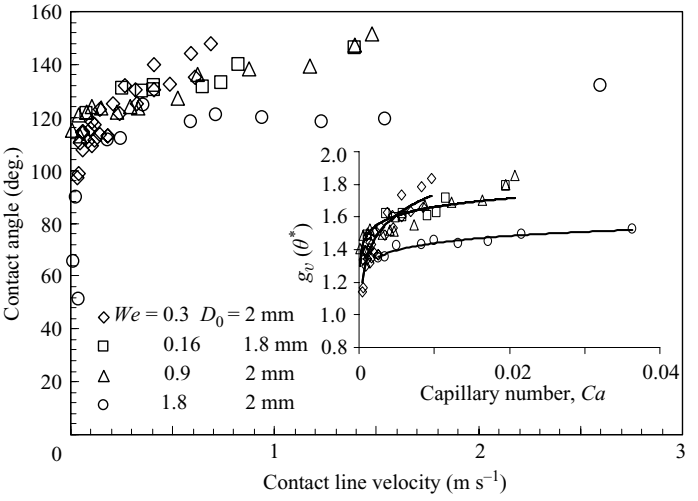


FIGURE 14. Contact angle variation with contact line velocity for water droplets 2.0 mm in diameter (nominal) impacting with $0.1 < We < 2.0$ on a partially wettable surface. The inset shows $g_v(\theta^*)$ versus the capillary number for the same data set and the solid line represents the Cox (1998) theory prediction ($1 \ll Re \ll L_H/L_S$) with adjusted inner region parameters.

We	L_S (m)	L_S (m)	θ_w (deg.)	θ_w (deg.)
	Kinematic stage	Final stage	Kinematic stage	Final stage
0.30	8.67×10^{-10}	2.27×10^{-12}	53	96
0.16	1.24×10^{-9}	1.61×10^{-11}	46	110
0.90	7.00×10^{-10}	4.73×10^{-13}	56	93
1.80	3.14×10^{-11}	1.65×10^{-15}	63	101

TABLE 4. Microscopic parameters obtained from the application of Cox's (1998) general Reynolds-number model to low-Weber-number water-droplet spreading on a partially wettable surface.

quantities rather than constant. We argue that at slow spreading (final stage), contact line motion can be strongly affected by surface heterogeneities and roughness. Cox's hydrodynamic model assumes an ideally smooth surface. In addition, the standard slip models do not include surface heterogeneities and are mainly phenomenological in nature. On the microscopic scale, there are two possible ways in which slip can occur. In the simple case of a solid wall, which is smooth on the molecular scale, molecular-dynamics simulations have shown that L_S is of the order of 10 Å (Cottin-Bizzone *et al.* 2004). On the other hand, for the more realistic case of a rough wall, slip can occur when the contact line 'jumps' across surface indentations. Jansons (1985) has shown that such jumps can give rise to the same macroscopic contact line–contact angle dynamics as slip does, but with a slip length that is inversely proportional to Ca. However, physically, the jump process is very different from the smooth-wall case, since the jerky motion of the contact line (resulting from the jumps) introduces a time-dependent contact line movement. Furthermore, there are two ways in which a 'jump' can occur. In one scenario, proposed by Joanny & Robbins (1990), the contact line is assumed to move very quickly through a trough, thus simulating a jump. In

https://doi.org/10.1017/S0022112006000231 Published online by Cambridge University Press

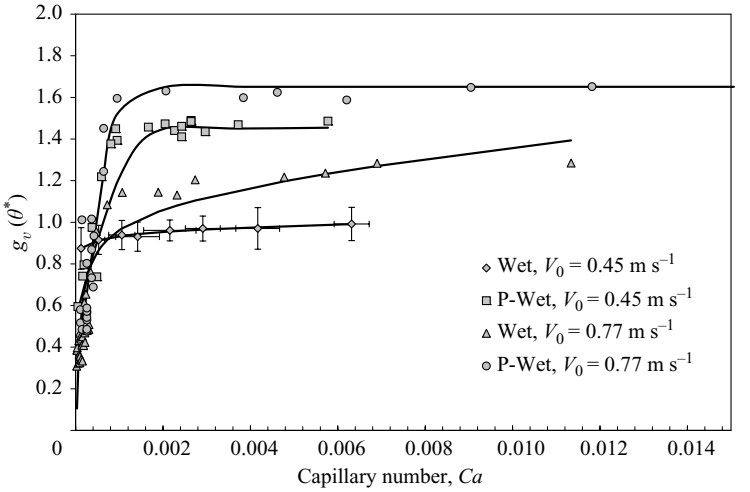


FIGURE 15. Application of Cox's (1998) theory (solid lines) for the general Reynolds-number case to the present experimental data for wettable (Wet) and partially wettable (P-Wet) surfaces. Corresponding Weber numbers are 3.9 for $V_0 = 0.45\,\mathrm{m\,s^{-1}}$, and 11.5 for $V_0 = 0.77\,\mathrm{m\,s^{-1}}$. The special function $g_v(\theta^*)$ is plotted against the capillary number to extract microscopic wetting parameters (L_S and θ_w; see table 5).

Target surface	*We*	θ_w (deg.) Kinematic stage	θ_w (deg.) Final stage	L_S (m) Kinematic stage	L_S (m) Final stage
Wettable	3.9	67.4	55.5	5.05×10^{-9}	–
Wettable	11.5	84.0	62.0	1.10×10^{-9}	–
Partially wettable	3.9	128.6	66.7	1.68×10^{-11}	–
Partially wettable	11.5	115.8	96.0	3.70×10^{-9}	–

TABLE 5. Microscopic parameters determined from Cox's (1998) general Reynolds-number model applied to water-droplet impacts with moderate Weber number on wettable and partially wettable surfaces. For the final spreading stages, no physically reasonable slip lengths were obtained.

the other case supported by Jansons (1985), the contact line can encounter points on the rough surface where the local force balance no longer holds, and the contact line jumps with capillary number $Ca \approx 1$ (slowed down only by the viscosity of the fluid). Whereas in the first scenario the slip length is still ~ 10 Å, in the second case the slip length can be of the order of the wall roughness or even larger.

Sheng & Zhou (1992) showed that even at small capillary numbers there exist significant discrepancies between the Cox model slip length predictions and their experimental data. They argued that the microscopic contact angle θ_w – and as a result the capillary force at the contact line – are actually contact line velocity dependent. By introducing a power-law velocity dependence, they were able to describe the experimental data with an optimum slip length of 0.5 µm, which is close to the surface roughness of the surfaces employed therein. Consider now the case of moderate Weber number droplet impact in figure 15, which shows $g_v(\theta^*)$ as a function of the capillary number for $We \gg 1$. For each condition, the theory was applied separately below and above a critical contact line velocity (likewise Ca) at which transition

https://doi.org/10.1017/S0022112006000231 Published online by Cambridge University Press

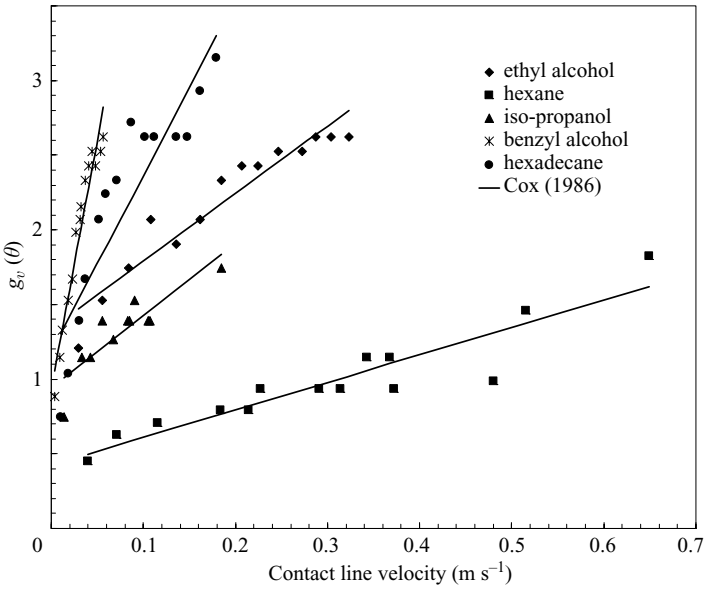


FIGURE 16. Dynamic contact angle variation of various liquids on nylon 6 (data of Ellison & Tejada 1970). The data are presented in terms of $g_v(\theta)$ versus V_{CL} in order to extract slip length (L_S) and microscopic contact angle (θ_w) values.

Liquid	L_S (m)	θ_w (deg.)	λ (nm)	κ_s (s^{-1})	ΔG_W (kJ mol^{-1})
Ethyl alcohol	2.00×10^{-7}	63.18	1.7	8.5×10^{9}	16.3
Hexane	2.98×10^{-8}	43.10	2.6	2.0×10^{11}	8.7
Iso-propanol	13.00×10^{-6}	56.20	1.9	5.4×10^{10}	11.7
Benzyl alcohol	4.46×10^{-14}	56.05	1.0	1.5×10^{12}	3.4
Hexadecane	5.00×10^{-8}	60.53	1.3	8.0×10^{9}	16.6

TABLE 6. Microscopic parameters (L_S, θ_w) obtained using Cox's (1986) theory applied to the experimental data of Ellison & Tejada (1970). Also shown are the corresponding molecular-kinetic parameters (λ, κ_S) for the same data.

from the kinematic spreading stage to the wetting-controlled final spreading stage occurs. Inspection of table 5, which lists the microscopic parameters extracted from the data of figure 15, reveals that the slip lengths determined from the kinematic spreading stage generally turn out to be $O \sim 10$ Å. On the other hand, slip lengths corresponding to the final stages of spreading turn out to be extremely small, i.e. $L_S \ll 10^{-15}$ m. This might suggest that the microscopic contact angles can be contact line velocity dependent in this regime regardless of the impact Weber number. This is also apparent from the observed strong dependence of the experimentally measured contact angle on contact line velocity during the final stages of spreading.

To further investigate the sensitivity of the slip length to the θ–V_{CL} variation, an analysis was performed on the data of Ellison & Tejada (1970). In particular, data sets showing spreading dynamics of various liquids on nylon were selected owing to the wide variations of contact angle with contact line velocity in these cases. Figure 16 shows $g_v(\theta)$ versus contact line speed for various liquids along with the prediction of Cox's theory (solid lines fitted to each data set). In this specific case, Cox

https://doi.org/10.1017/S0022112006000231 Published online by Cambridge University Press

(1986)'s theory was applied as there were no initial inertial effects in the corresponding experiments. The same curves were also fitted with the molecular kinetic theory (not shown in the figure). Table 6 summarizes the microscopic parameters obtained using Cox's theory from the data in figure 16 together with the corresponding molecular kinetic parameters. There appears to be no direct correlation between the slip length extracted from the theory and the specific θ–V_{CL} relationship. However, if the contact angle is strongly dependent on the contact line velocity at speeds $V_{CL} < 0.1\,\mathrm{m\,s^{-1}}$, slip lengths below molecular scales are obtained (see benzyl alcohol values in table 6). This and the previous experimental results clearly indicate that in the slow regime of forced spreading, the slip length – and consequently the microscopic contact angle – are contact line velocity dependent. Molecular simulations in support of this observation have been published (Cottin-Bizzone *et al.* 2004). Such studies indicate that slip length is strongly influenced by surface roughness as well as by contact line speed. In particular, Cottin-Bizzone *et al.* (2004) found that dynamic slip lengths decline as the hydrodynamic spreading pressure reduces from an initially high value towards the capillary pressure ($P_{cap} \sim 2\sigma\cos\theta/L_S$), when the liquid starts to invade surface grooves (strong solid/liquid interactions). Similar conclusions have appeared in the literature especially for polar liquids spreading on low-energy surfaces. Hayes & Ralston (1993) and Petrov & Petrov (1992) compared measured dynamic contact angles for water/glycerol solutions spreading on low-energy polyethylene terephthalate (PET) surfaces with values obtained from Cox (1986). Predictions and measurements compared favourably, although the hydrodynamic model produced slip lengths smaller than molecular dimensions.

According to the aforementioned results, application of the Cox theory to droplet impact spreading with strong liquid/solid interactions requires prior knowledge of the functional dependence of θ_w on V_{CL}, which is practically difficult to derive. On the other hand, Cox's theory performs well during kinematic spreading, in which solid/liquid interactions are weaker.

The molecular-kinetic parameters for the data of Ellison & Tejada (1970) (table 6) compare favourably with other literature data on forced spreading of low-viscosity liquids. Solid–liquid interaction frequencies κ_s for the liquids shown in table 6 range from 10^9 to $10^{12}\,\mathrm{s^{-1}}$. This range contains the value $10^{10}\,\mathrm{s^{-1}}$ reported by Blake & Ruschak (1997) for low-viscosity fluids impacting on polyester surfaces. The rapid changes in $\theta - Ca$ slope seen therein at a specific capillary number imply a change in wetting mechanism (similar to the data in figure 14). Blake & Ruschak (1997) reported that neither molecular-kinetic theory nor hydrodynamic theory could describe the entire data range with a single set of adjustable parameters. This is because at low wetting speeds, strong solid–liquid interactions dominate the wetting process (low values of κ_s), whereas at high wetting speeds, the solid/liquid molecular interactions are weak owing to the inability of the molecules to relax within the available time in the fast-moving flow. As postulated in Blake & Ruschak (1997), the locus of molecular motion as the liquid spreads over the solid surface shifts away from the surface to a plane above the absorbed liquid layer, where the influence of the solid is reduced, in turn raising the value of κ_s.

4.5. *Application of the molecular-kinetic theory*

Figure 17 compares the dependence of dynamic contact angle on contact line speed for 1.4 mm diameter droplets impinging on wettable and non-wettable substrates. The solid lines represent the molecular-kinetic theory fit to the data. On the wettable surface with $V_0 = 0.45\,\mathrm{m\,s^{-1}}$ ($We = 3.9$), the advancing contact angle increases with

https://doi.org/10.1017/S0022112006000231 Published online by Cambridge University Press

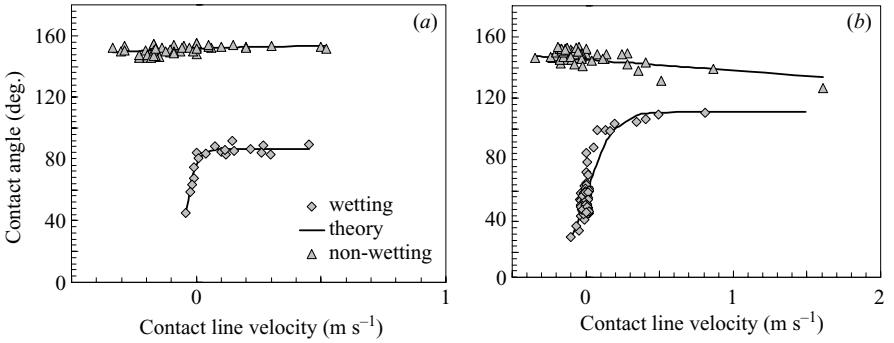


FIGURE 17. Comparisons between dependence of contact angle on contact line speed for 1.4 mm diameter droplets impinging on wettable ($\theta_E = 20°$) and non-wettable ($\theta_E = 164°$) surfaces. (*a*) $V_0 = 0.45\,\mathrm{m\,s^{-1}}$ ($We = 3.9$), (*b*) $V_0 = 0.77\,\mathrm{m\,s^{-1}}$ ($We = 11.5$). The solid lines represent the molecular kinetic (M-K) theory fit to the data (see table 7).

contact line speed (figure 17*a*). Impact with $V_0 = 0.77\,\mathrm{m\,s^{-1}}$ ($We = 11.5$) shows a very similar contact-angle dependence on contact line velocity (figure 17*b*). On the non-wettable surface in figure 17(*b*), the advancing contact angle slightly decreases with increasing contact line speed. The receding contact angle, on the other hand, does not depend on the receding contact line speed in figure 17(*b*). It is worth noting that contact line speed at the early stages of spreading exceeds the impact velocity for both conditions. The non-wetting curve in figure 17(*a*) shows that when the impact inertia is lowered ($V_0 = 0.45\,\mathrm{m\,s^{-1}}$) the diminishing trend of the advancing contact angle disappears. The advancing contact angle does not change with increasing contact line speed. The receding contact angle is independent of the receding contact line speed, similar to the trend shown in figure 17(*b*). Elliott & Ford (1972) measured dynamic contact angles, spreading rate and height of water and a number of alcohol droplets ($D_0 = 2\,\mathrm{mm}$, $V_0 = 1.67\,\mathrm{m\,s^{-1}}$) impacting on a partially wettable smooth wax surface. One of their major conclusions was that during the inertia-controlled spreading stage, the contact angle remained constant regardless of the type of fluid or the contact line speed.

In the case of a wettable substrate in figure 17(*a*), contact angle hysteresis is approximately 25°, whereas in figure 17(*b*), contact angle hysteresis is approximately 50°. On the non-wettable surface, however, contact angle hysteresis is practically zero, because the dynamic contact angle is independent of advancing and receding contact line speeds. Similar observations by Fukai *et al.* (2000) at substrate temperatures below the Leidenfrost temperature (a critical surface temperature at which film boiling takes place, thus lifting the droplet from the hot surface) showed that advancing contact angle increased with increasing contact line velocity. However, above the Leidenfrost temperature, both advancing and receding contact angles were independent of the contact line speed (resembling the dynamics on a non-wettable surface).

In figure 18, the corresponding θ–V_{CL} curves for partially wetting dynamics are presented for two impact velocities; $V_0 = 0.77\,\mathrm{m\,s^{-1}}$, and $V_0 = 0.45\,\mathrm{m\,s^{-1}}$. In this figure, the first and second spreading cycles are separated for clarity. The advancing contact angle changes only slightly with contact line speed during the first and second advancing cycles for both impact conditions. On the other hand, the receding contact angle decreases with increasing receding contact line speed in each case. On a partially wettable surface, spreading dynamics is quite complicated because of multiple advancing and receding motions of the contact line. Secondary spreading

https://doi.org/10.1017/S0022112006000231 Published online by Cambridge University Press

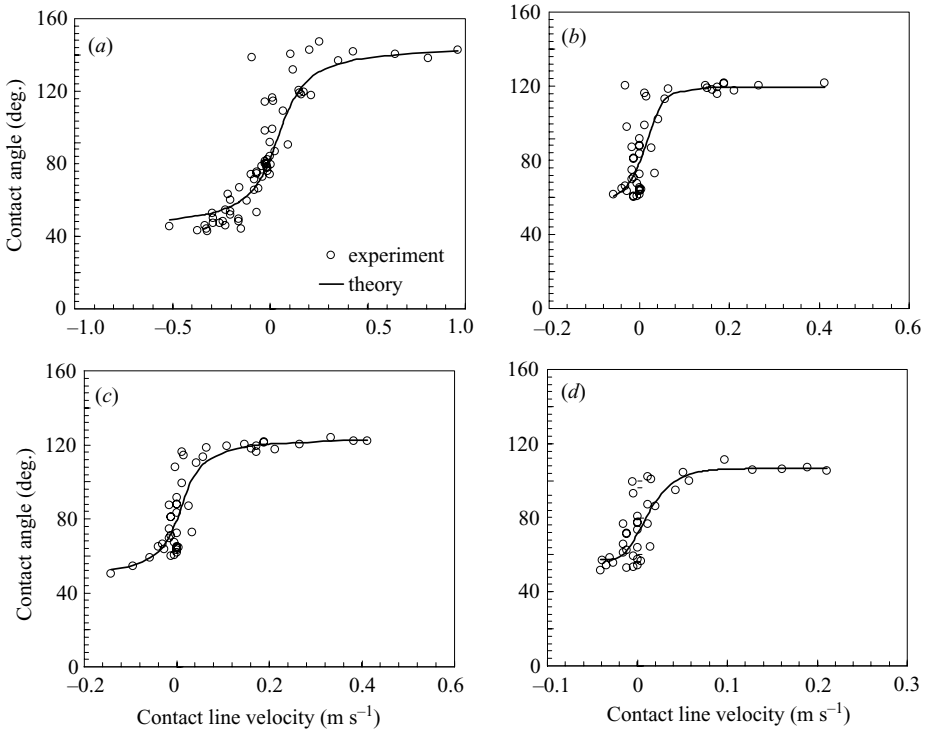


FIGURE 18. θ *vs.* V_{CL} comparisons among experimental data and molecular theory of wetting predictions from (2.12) on a partially wettable ($\theta_E = 73^\circ$) surface. In all cases, $D_0 = 1.4$ mm. (*a*) First spreading–receding cycle with $V_0 = 0.77\,\mathrm{m\,s^{-1}}$ ($We = 11.5$). (*b*) Second spreading–receding cycle with $V_0 = 0.77\,\mathrm{m\,s^{-1}}$. (*c*) First spreading–receding cycle with $V_0 = 0.45\,\mathrm{m\,s^{-1}}$ ($We = 3.9$). (*d*) Second spreading–receding cycle with $V_0 = 0.45\,\mathrm{m\,s^{-1}}$.

does not occur always when the droplet recoils on partially wettable surfaces. The second spreading cycle is strongly dependent on the equilibrium contact angle of a given liquid/solid system. We observed that on fluorinated polymer surfaces, such as Teflon and paraffin wax, secondary spreading is very common for droplet impact with $We > 5$ and $\theta_E > \pi/2$. Analysis of figure 18 indicates that for $V_0 = 0.77\,\mathrm{m\,s^{-1}}$, contact angle hysteresis during the first spreading cycle is roughly 70°, whereas it is roughly 60° during the second spreading cycle. Similarly, for $V_0 = 0.45\,\mathrm{m\,s^{-1}}$, contact angle hysteresis during the first spreading cycle is 60° and during the second spreading cycle, it is 45°. Elliott & Ford (1972) investigated the effect of a pre-wetted wax surface on contact angle dynamics of impacting water drops ($D_0 \sim 2$ mm and $V_0 \sim 2\,\mathrm{m\,s^{-1}}$) and found that the dynamic contact angle during the second spreading cycle does not pass through the same minima and maxima as in the first cycle. This was attributed to an adsorbed layer of molecules, which can exert a surface pressure proportional to $(\sigma_{SS} - \sigma_{SV})$, where σ_{SS} denotes surface energy of the solid substrate and σ_{SV} is the solid–vapour surface energy. Formation of a thin liquid film is a plausible reason for the observed complex contact angle dynamics on partially wettable surfaces (Yarin, Liu & Reneker 2002).

Figures 17 and 18 also show the molecular-kinetic theory predictions with adjusted molecular parameters κ and λ. Overall, the fit is better for the wettable ($\theta_E = 20^\circ$) and the partially-wettable ($\theta_E = 73^\circ$) data sets, as compared to the non-wettable

https://doi.org/10.1017/S0022112006000231 Published online by Cambridge University Press

Target surface	V_0 (m s^{-1})	κ_w (10^6 s^{-1})	κ_s (10^{11} s^{-1})	λ (nm)	θ_E (deg.)	$\Delta G_W = (\Delta G_S + \Delta G_V)$ (kJ mol^{-1})	$\Delta G_S/\Delta G_V$
Wettable	0.77	4.20	1.9	2.4	20	19.6	0.6
Wettable	0.45	1.20	0.6	3.4	20	16.4	1.6
Partially wettable (first spreading)	0.77	3.00	1.3	1.0	73	18.6	0.7
Partially wettable (second spreading)	0.77	1.10	0.5	1.1	73	16.2	1.6
Partially wettable (first spreading)	0.45	1.20	54	1.1	73	27.8	0.6
Partially wettable (second spreading)	0.45	0.87	37	1.1	73	26.9	0.7

TABLE 7. Molecular-kinetic wetting theory parameters obtained from fitting (2.12) to the experimental data plotted in figures 17 and 18. First and second spreading cycle dynamics on the partially wettable surface were analysed separately. θ_E was measured experimentally using the sessile droplet method.

($\theta_E = 164^\circ$) cases. The curves for the non-wettable data did not yield physically reasonable molecular parameters. Molecular-kinetic parameters obtained from the curve-fitting procedure for the wettable and partially wettable data of figures 17 and 18 are presented in table 7. The molecular-kinetic parameter κ_s corresponding to forced water spreading on polyethylene terephthalate (PET) surfaces reported by Hayes & Ralston (1993) compare reasonably well with the data reported in table 7. According to Schwartz & Tejada (1972), at high contact line speeds the reciprocal of the liquid molecular oscillation frequency (κ_s^{-1}) over the adsorption sites of the target surface should be of the same order of magnitude as the escape time τ of a water molecule in the bulk phase ($\tau \approx 10^{-11}$ s). This is confirmed by the present values of $\kappa_s \sim O(10^{11})\,\mathrm{s}^{-1}$ given in table 7. Moreover, as seen in table 7, the curve fit results indicate $\lambda \approx 1$ nm, which is close to the diameter of a water molecule. This suggests a low probability of the water molecules adsorbing/desorbing onto/from the solid surface. Instead, the molecular transitions from a given potential well to the adjacent one most probably correspond to Eyring's model of bulk viscous friction (Glasstone *et al.* 1941; Bird, Stewart & Lightfoot 1960). The calculated values of ΔG_W (from (2.7)) for the wettable and partially wettable surfaces are also given in table 7. The magnitude of ΔG_W is related to the energy required for the contact line to move across the solid surface. High or low values of ΔG_W imply, respectively, strong or weak velocity dependence of the contact angle, as discussed in § 2.2. For systems where the liquid is likely to interact strongly with the solid target, for example, aqueous glycerol drops on glass substrates, $\Delta G_W \approx 40\,\mathrm{kJ\,mol^{-1}}$. However, when liquid/solid interactions are comparatively weak, for example, silicon fluids on glass substrates, ΔG_W is lower $\approx 10\,\mathrm{kJ\,mol^{-1}}$ (Blake 1993). The present values of ΔG_W in table 7 fall between these two limits, implying that liquid/liquid and liquid/surface interactions are of equal importance. Further evidence is obtained from the corresponding values of the ratio $\Delta G_S/\Delta G_V$, as shown in table 7. Note that in all solid/liquid systems of the current study it is $0.5 < \Delta G_S/\Delta G_V < 2$, therefore, neither solid/liquid interactions nor liquid/liquid effects dominate contact line dynamics thoroughly. At high equilibrium contact angles ($\theta_E \geqslant 140^\circ$, i.e. low-energy surfaces), the molecular wetting theory predicts the contact angle/contact line speed trend shown by the solid lines in figure 17. At this stage, it is not clear whether this theory can be used to describe spreading

https://doi.org/10.1017/S0022112006000231 Published online by Cambridge University Press

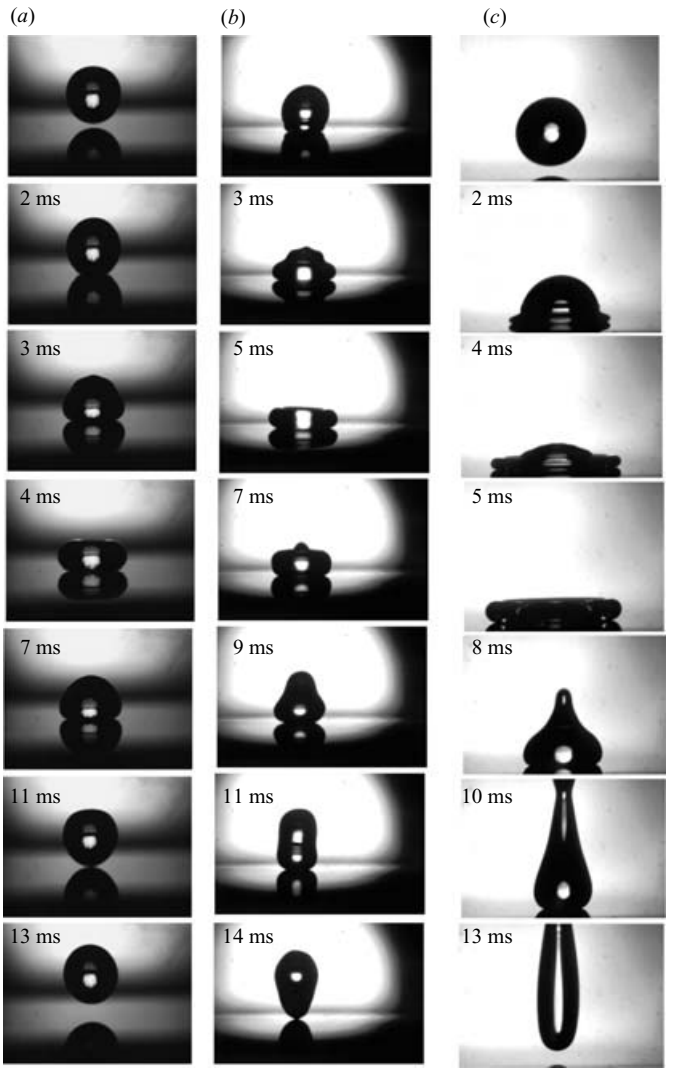


FIGURE 19. (*a*) Impact and rebound of a 1.43 mm diameter water droplet on a non-wettable surface ($V_0 = 0.15\,\mathrm{m\,s^{-1}}$, $We = 0.44$, $D_m/D_0 = 1.25$, $V' = 0.14\,\mathrm{m\,s^{-1}}$, $\epsilon = 0.93$). (*b*) Impact and rebound of a 1.47 mm water droplet on a non-wettable surface ($V_0 = 0.28\,\mathrm{m\,s^{-1}}$, $We = 1.59$, $D_m/D_0 = 1.46$, $V' = 0.25\,\mathrm{m\,s^{-1}}$, $\epsilon = 0.89$). (*c*) Impact and rebound of a 1.41 mm water droplet on a non-wettable surface ($V_0 = 0.65\,\mathrm{m\,s^{-1}}$, $We = 8.1$, $D_m/D_0 = 2$, $V' = 0.56\,\mathrm{m\,s^{-1}}$, $\epsilon = 0.86$).

behaviour on non-wettable surfaces, where complete droplet rebound is observed. On such ultra-hydrophobic surfaces, droplets impact the solid target without wetting it, eventually bouncing with considerable elasticity.

4.6. *Rebound dynamics on non-wettable surfaces*

Figure 19 displays three impact sequences corresponding to water droplets striking a non-wettable surface with $V_0 = 0.15\,\mathrm{m\,s^{-1}}$, $0.28\,\mathrm{m\,s^{-1}}$ and $0.65\,\mathrm{m\,s^{-1}}$, respectively. In all three cases, rebound occurred. The impact restitution coefficient is defined as $\epsilon = V'/V_0$, with V' being the droplet velocity after bounce off. ϵ offers a measure of droplet kinetic energy loss during impact, spreading and recoil. For the three cases

https://doi.org/10.1017/S0022112006000231 Published online by Cambridge University Press

in figure 19, the respective rebound velocities V' were $0.14\,\mathrm{m\,s^{-1}}$ ($\epsilon = 0.93$), $0.25\,\mathrm{m\,s^{-1}}$ ($\epsilon = 0.89$), and $0.56\,\mathrm{m\,s^{-1}}$ ($\epsilon = 0.86$). Although droplet residence time on the surface (13 ms) was not affected by the impact speed in figure 19, droplet deformation was seen to increase considerably as the droplet initial impact speed was increased from (*a*) to (*c*). As reported by Richard & Quéré (2000), the restitution coefficient ϵ can be as high as 0.9 for droplet impact on highly non-wettable solid surfaces with $We < 1$. Their experiments with $D_0 = 0.5\,\mathrm{mm}$, $V_0 = 0.2\,\mathrm{m\,s^{-1}}$ on non-wettable substrates featured advancing and receding contact angles close to 170° with small contact angle hysteresis. The impacts shown in figure 19, with Weber numbers at the high end or above the range considered by Richard & Quéré (2000), have ϵ in the range 0.86–0.93. In addition, for the non-wetting impacts of figure 17(*a*) and 17(*b*), ϵ was found to be 0.85 and 0.79, respectively. For an ideal elastic rebound $\epsilon = 1$, i.e. no energy is lost. In the present study, water droplets impacting with $We = 0.4$–12 on non-wettable surfaces have ϵ in the range 0.79–0.93, and thus seem to lose a measurable amount of energy upon rebound. When a drop strikes a surface, the most natural mechanism of dissipation is liquid viscosity. However, on strongly non-wettable surfaces viscous dissipation is practically negligible. Thus, this mechanism cannot be responsible for the rebound energy losses in the current experiments. According to Richard & Quéré (2000), increasing contact angle hysteresis on non-wettable surfaces causes a less elastic droplet rebound (i.e. lower ϵ). Thus, droplets showing very small dynamic contact angle hysteresis on a specific non-wettable surface are more likely to rebound. However, as seen in figure 17, contact angle hysteresis on the present non-wettable surfaces was minimal, thus contact angle hysteresis cannot be responsible for the energy losses seen at rebound. It is noted that even with no contact angle hysteresis, Richard & Quéré (2000) found restitution coefficients lower than 1, indicating a separate mechanism of energy dissipation, namely the transfer of initial kinetic energy to drop vibrations after the droplet bounced off the surface. This is believed to be the mechanism of energy dissipation for the current experiments as well.

Numerical studies on droplet rebound corroborate the dependence of restitution coefficient on droplet impact Weber number (Nobari, Jan & Tryggvason 1996). Head-on collisions of two similar drops resemble the collision of a drop with a flat wall if full slip boundary conditions are assumed at the wall and wetting effects are ignored. Nobari *et al.* (1996) studied the head-on collision of equal sized drops by numerical simulations in the range $2 < We < 115$. The Weber number was found to be the controlling parameter of the collision and bounce-back dynamics. The restitution coefficient was approximately 0.8 for Weber numbers less than 15, and declined to 0.4 for Weber numbers above 90.

Interaction of water droplets with ultra-hydrophobic surfaces is a problem of both practical and theoretical interest. Experimentally, when the response of a resting drop to a tilt of the surface is investigated, it is found that all super-hydrophobic surfaces are not equivalent. In some cases, the drop readily rolls off the surface, while in other cases the drop clings to the surface, even for high tilt angles. Quéré (2002) refers to these two contrasting cases as 'slippery' and 'sticky' super-hydrophobic surfaces. Wettability of such surfaces by water is governed not only by chemical properties but also by the nanotexture of the surface. Proper nanotexturing of a non-wettable surface enhances its hydrophobicity (Richard & Quéré 2000; Quéré 2002). Two main wetting modes described by the Wenzel (1936) and Cassie & Baxter (1944) theories have been frequently examined for solids with specific surface textures. These theories can be useful, having been successfully implemented to describe the thermodynamics

https://doi.org/10.1017/S0022112006000231 Published online by Cambridge University Press

of unique wetting regimes observed on super-hydrophobic surfaces. In connection with these theories, wetting on rough surfaces can be classified in one of the following two regimes:

(i) Wenzel regime, where the solid/liquid interface faithfully follows the solid roughness, and

(ii) Cassie–Baxter or air-pocket regime, where air patches are confined between the liquid and the solid.

In the Cassie–Baxter model, a drop rests on the peaks of surface protrusions and bridges the air gaps in between. In the Wenzel model, the liquid droplet retains contact at all points with the solid surface below it. In this section, we analyse the wetting dynamics on the present non-wettable surfaces based on the Wenzel and Cassie–Baxter theories.

On a flat, smooth and chemically homogeneous surface, the equilibrium contact angle θ_E, is given by Young's equation

$$\cos\theta_E = \frac{\sigma_S - \sigma_{SL}}{\sigma_L}, \tag{4.3}$$

where σ_L is the liquid–vapour surface tension and the subscripts S and SL refer to the solid–vapour and solid–liquid interfacial tensions, respectively. When the surface is roughened, Young's equilibrium contact angle can no longer be described by (4.3). The actual contact angle can be approximated by either the Wenzel (1936) or the Cassie & Baxter (1944) models. Namely, the Wenzel contact angle on a rough surface is

$$\cos\theta_E^W = r\cos\theta_E, \tag{4.4}$$

while the Cassie–Baxter contact angle is given by

$$\cos\theta_E^{CB} = \phi_s\cos\theta_E - (1-\phi_s), \tag{4.5}$$

depending on whether intimate contact between the liquid and the solid at all points below the drop is maintained (4.4), or air-bridging at some points below the drop exits (4.5). In these formulae, r is the surface roughness, defined as the ratio of the true surface area to the horizontal projection of the surface area. ϕ_s is defined as the solid fraction upon which the droplet rests. The Wenzel model predicts that surface roughness enhances the equilibrium contact angle when $\theta_E > \pi/2$. However, the enhancement due to roughness, as predicted by the Wenzel or Cassie–Baxter models, can show significant differences owing to their different treatment of liquid–solid interface morphology. To visualize the effect of these two wetting mechanisms on contact angle, consider figure 20 in which Wenzel and Cassie–Baxter contact angles are shown against the corresponding smooth surface values. In the case of Cassie–Baxter wetting, decreasing surface solid fraction ϕ_S, i.e. increasing surface roughness, causes higher contact angles. In the Wenzel regime, increasing surface roughness reduces wettability on surfaces with $\theta_E > 90^o$, while it enhances wettablity on surfaces with $\theta_E < 90^\circ$.

The non-wettable surfaces used in the current experiments had fractal surface structures. Data from a detailed static contact angle study on the non-wettable surfaces provided by Kao (Japan) indicated that a freshly prepared AKD (alkylketene dimer) surface has a water equilibrium contact angle of 123° (corresponding to a smooth surface), whereas after heat curing for 60 h, the contact angle reached 164° (Shibuichi, personal communication). Heat treatment caused fractal surface structures to form, thus creating a rough surface. Inspection of the non-wettable $\theta - V_{CL}$ data in

https://doi.org/10.1017/S0022112006000231 Published online by Cambridge University Press

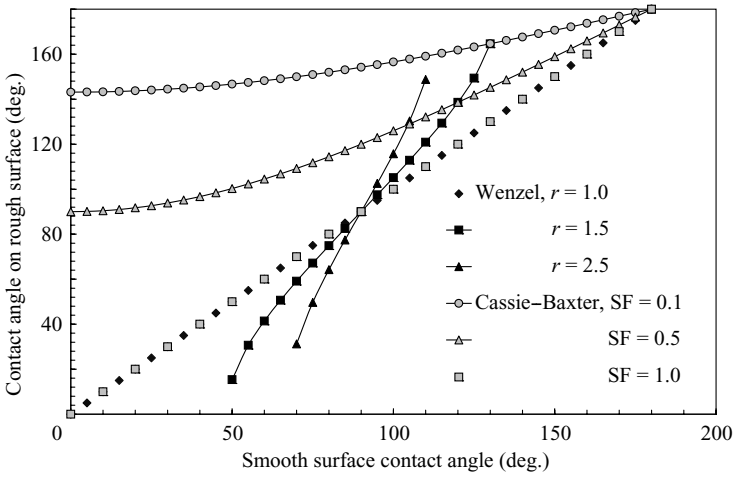


FIGURE 20. Contact angle on a rough surface against its counterpart on an ideal smooth surface made of the same material. Wenzel and Cassie–Baxter curves are shown for varying surface roughness r and contact solid fraction (ϕ_S or SF).

figure 17 also indicated advancing contact angles of about 158°, confirming the chosen equilibrium value of 164°. To classify the wetting mode of the present non-wettable surfaces, equations (4.4) and (4.5) have been combined to obtain a critical contact angle θ^{CR} at which transition from Wenzel wetting to Cassie–Baxter wetting occurs (Quéré 2002). It is

$$\cos\theta^{CR} = \frac{\phi_S - 1}{r - \phi_S}. \tag{4.6}$$

Comparison of the experimentally measured equilibrium contact angle with θ^{CR} can indicate which wetting regime is applicable. Equilibrium contact angles below θ^{CR} correspond to Wenzel wetting, while angles above θ^{CR} imply Cassie–Baxter wetting. The employed AKD surface before the curing process is smooth and the equilibrium contact angle at this stage is $\theta_E = 123°$. The final equilibrium contact angle on the heat-roughened surface was measured to be 164°. Assuming Cassie–Baxter wetting and using (4.5), the percentage of the solid in contact with liquid can be calculated to be $\phi_S = 0.085$. With $\phi_S = 0.085$, the critical contact angle for $r = 2.3$ (Shibuichi *et al.* 1998) is calculated to be 114.4° from (4.6). Since the equilibrium contact angle of water on the heat-roughened non-wettable surface is larger than the critical contact angle, it is confirmed that the Cassie–Baxter model best describes the non-wettable surfaces employed herein. This means that as the droplets spread on the non-wettable surfaces, partial liquid/solid contact is maintained.

5. Conclusions

An experimental study has been presented on contact angle dynamics during impact spreading/recoiling of mm sized water droplets impacting orthogonally on various surfaces with $We = O(0.1) - O(10)$, $Ca = O(0.001) - O(0.01)$, $Re = O(100) - O(1000)$, $Oh = O(0.001)$ and $Bo = O(0.1)$. In this impact regime, inertial, viscous and capillary phenomena act in unison to influence contact line motion and arrest, as well as contact angle dynamics. The target surfaces were classified as wettable (equilibrium contact angles $\theta_E < 40°$), partially wettable ($40° < \theta_E < 140°$), to non-wettable ($\theta_E > 140°$). By

https://doi.org/10.1017/S0022112006000231 Published online by Cambridge University Press

correlating the temporal behaviours of apparent (macroscopic) contact angle θ and contact-line speed V_{CL}, the angle *vs.* speed relationship was established for each case examined. The present experiments – featuring both accelerating and decelerating wetting lines – offer an attractive platform to resolve contact angle dependence on contact line speed (or its temporal rate of change). Most of the impacts revealed the early presence of capillary waves on the droplet free surface; these waves dissipated within $O(1\,\text{ms})$ and had structures similar to those predicted by Renardy *et al.* (2003). In view of the dynamic wetting theories considered, the respective $\theta - V_{CL}$ data of Ellison & Tejada (1970) and Schwartz & Tejada (1970, 1972) have also been processed to provide additional insight.

The present data showed that maximum droplet spreading remain relatively insensitive to surface wettability (θ_E), with peak spreading diameters for different substrates (wetting to non-wetting) collapsing into a single curve $D_m/D_0 \sim V_0^{2/7}$. This correlation shows a higher sensitivity to impact speed than earlier spreading correlations $D_m/D_0 \sim V_0^{1/5}$ for viscous liquids, but less than the recent correlation $D_m/D_0 \sim V_0^{1/2}$ suggested by Clanet *et al.* (2004). The difference is attributed to liquid–solid interactions, which are shown to be more pronounced in the lower Weber number range applicable to the present work.

At Weber numbers in the range $1 < We < 40$, temporal monitoring of θ displayed well-structured oscillations around the respective equilibrium (θ_E) values, and revealed that surface wettability has a critical influence on contact angle dynamic behaviour, with increased wettability resulting in higher frequency and lower oscillation magnitude. For the partially wettable surfaces, the results showed that impact inertia has practically no influence on contact angle dynamics in this regime. For the wettable surfaces, the effect of inertia also appeared to be limited. At low Weber numbers ($We < 1$), the results confirmed that surface wettability strongly affects contact angle dynamics. In this case, impact inertia did affect both frequency and amplitude of contact line oscillations.

Contact angle hysteresis was present during impact on wettable and partially wettable surfaces, and was found to decrease with reduced impact inertia. On non-wettable surfaces, contact angle hysteresis was practically zero. Impact on non-wettable surfaces, which was followed by complete rebound, showed that both advancing and receding contact angle values did not vary with contact line speed, thus suggesting a tank tread (rolling) mechanism. A slightly diminishing contact angle/contact line speed trend was observed for the advancing stages of non-wettable impacts with $We \sim 10$. Using the hydrodynamic theory of Cox (1998) with adjustable parameters (microscopic contact angle θ_w and slip length L_S) to fit the experimental data suggested that both θ_w and L_S should be contact line velocity dependent in the slow spreading regime. The hydrodynamic theory performed well during kinematic (fast) spreading, in which solid/liquid interactions are weak. The molecular theory of wetting by Blake & Haynes (1969) was shown to model adequately the observed dependence of the advancing/receding contact angle on contact line speed on the wettable and partially wettable surfaces. The procedure showed that under forced spreading conditions, solid/liquid and liquid/liquid interactions compete in retarding liquid front advancement. However, additional work is required to establish a link between the molecular theory of wetting and the experimentally observed contact angle/contact line speed relationship on the non-wettable surfaces, where complete droplet rebound occurred. Cassie–Baxter (partial) liquid/solid contact was shown to be dominant during impact on the non-wettable surfaces. The corresponding restitution coefficients were in the range 0.79–0.93, thus suggesting that the present droplets striking

https://doi.org/10.1017/S0022112006000231 Published online by Cambridge University Press

non-wettable surfaces lose a measurable amount of energy upon rebound. This apparent energy loss was attributed to the transfer of initial kinetic energy to in-flight drop vibrations after the droplet bounced off the surface.

This work was supported by NASA grant NAG3-2456. Useful discussions with Dr Alexander Yarin and Dr Terence Blake (retired from Kodak European R & D, UK) are acknowledged with appreciation. The authors are indebted to Dr Hilton Lewis (MIT), Dr Karen Gleason (MIT) and Dr S. Shibuichi (Japan) for providing some of the super-hydrophobic surfaces employed in the experiments. Brian Sautter's assistance in data processing is also acknowledged.

REFERENCES

Attinger, D., Zhao, Z. & Poulikakos, D. 2000 An experimental study of molten microdroplet surface deposition and solidification: transient behavior and wetting angle dynamics. *Trans. ASME* C: *J. Heat Transfer* **122**, 535–550.

Bergeron, V., Bonn, D., Martin, J. Y. & Vovelle, L. 2000 Controlling droplet deposition with polymer additives. *Nature* **405**, 772–775.

Bird, R. B., Stewart, W. E. & Lightfoot, E. N. 1960 *Transport Phenomena*. John Wiley.

Blake, T. D. 1993 Dynamic contact angles and wetting kinetics. In *Wettability* (ed. J. C. Berg), pp. 251–260. Marcel Dekker.

Blake, T. D. & Haynes, J. M. 1969 Kinetics of liquid/liquid displacements. *J. Colloid Interface Sci.* **30**, 421–423.

Blake, T. D. & Ruschak, K. J. 1997 Wetting: static and dynamic contact lines. In *Liquid Film Coating* (ed. S. F. Kistler & P. M. Schweizer). Chapman & Hall.

Cassie, A. B. D. & Baxter, S. 1944 Wettability of porous surfaces. *Trans. Faraday Soc.* **40**, 546–549.

Clanet, C., Beguin, C., Richard, D. & Quéré, D. 2004 Maximal deformation of an impacting drop. *J. Fluid Mech.* **517**, 199–208.

Clift, R., Grace, J. R. & Weber, M. E. 1978 *Bubbles, Drops and Particles*. Academic.

Cottin-Bizzone, C., Barentin, C., Charlaix, E., Bocquet, L. & Barrat, J.-L. 2004 Dynamics of simple liquids at heterogeneous surfaces: molecular-dynamics simulations and hydrodynamic description. *Eur. Phys. J.* E **15**, 427–438.

Cox, R. G. 1986 The dynamics of the spreading of liquids on a solid surface. Part 1. Viscous flow. *J. Fluid Mech.* **168**, 169–194.

Cox, R. G. 1998 Inertial and viscous effects on dynamic contact angles. *J. Fluid Mech.* **357**, 249–278.

Davis, S. H. 1983 Contact line problems in fluid mechanics. *J. Appl. Mech.* **50**, 977–982.

Dussan, E. B. 1979 On the spreading of liquids on solid surfaces: static and dynamic contact lines. *Annu. Rev. Fluid Mech.* **11**, 371–400.

Dussan, E. B. & Davis, S. H. 1974 On the motion of a fluid/fluid interface along a solid substrate. *Phys. Fluids* **65**, 71–80.

Elliott, T. A. & Ford, D. M. 1972 Dynamic contact angles: impact spreading of water drops in air and aqueous solutions of surface active agents in vapor on smooth paraffin surfaces. *Trans. Faraday Soc.* I **68**, 1814–1823.

Ellison, A. H. & Tejada, S. B. 1970 Dynamic liquid/solid contact angles and films on contaminated mercury. Report. Contract: NAS 3-9705. NASA, Cleveland, OH.

Ford, R. E. & Furmidge, C. G. L. 1967 Impact and spreading of spray drops on foliar surfaces. *Wetting, Soc. Chem. Indust. Mono.* **25**, 417–433.

Fukai, J., Shiiba, Y., Yamamoto, T., Miyatake, O., Poulikakos, D., Megaridis, C. M. & Zhao, Z. 1995 Wetting effects on the spreading of a liquid droplet colliding with a flat surface: experiment and modelling. *Phys. Fluids* **7**, 236–247.

Fukai, J., Etou, M., Asanoma, F. & Miyatake, O. 2000 Dynamic contact angles of water droplets sliding on inclined hot surfaces. *J. Chem. Engng Japan* **33**, 177–179.

Gao, F. Q. & Sonin, A. A. 1994 Precise deposition of microdrops: the physics of digital microfabrication. *Proc. R. Soc. Lond.* A **444**, 533–554.

de Gennes, P. G. 1985 Wetting: statics and dynamics. *Rev. Mod. Phys.* **57**, 827–842.

https://doi.org/10.1017/S0022112006000231 Published online by Cambridge University Press

Glasstone, S., Laidler, K. & Eyring, H. 1941 *The Theory of Rate Process*. McGraw–Hill.

Hatta, N., Fujimoto, H. & Takuda, H. 1995 Deformation process of a water droplet impinging on a solid surface. *Trans. ASME* I: *J. Fluids Engng* **117**, 394–401.

Hayes, D. J., Wallace, D. B., Boldman, M. T. & Marusak, R. E. 1993 Picoliter solder droplet dispensing. *Intl J. Microcircuits Electron. Packaging* **16**, 173–180.

Hayes, R. A. & Ralston, J. 1993 Forced liquid movement on low energy surfaces. *J. Colloid Interface Sci.* **159**, 429–438.

Huh, E. & Scriven, L. E. 1971 Hydrodynamic model of steady movement of a solid/liquid/fluid contact line. *J. Colloid Interfcae Sci.* **35**, 85–90.

Jansons, K. M. 1985 Moving contact lines on a two-dimensional rough surface. *J. Fluid Mech.* **154**, 1–28.

Joanny, J. F. & Robbins, M. O. 1990 Motion of a contact line on a heterogeneous surface. *J. Chem. Phys.* **92**, 3206–3212.

Kistler, S. F. 1993 Hydrodynamics of wetting. In *Wettability* (ed. J. C. Berg). Dekker.

Nobari, M. R., Jan, Y.-J. & Tryggvason, G. 1996 Head-on collision of drops: a numerical investigation. *Phys. Fluids* **8**, 29–42.

Okumura, K., Chevy, F., Richard, D., Quéré, D. & Clanet, C. 2003 Water spring: a model for bouncing drops. *Europhys. Lett.* **62**, 237–243.

Orme, M. E., Huang, C. & Courter, J. 1996 Precision droplet-based manufacturing and material synthesis: fluid dynamics and thermal control issues. *Atomiz. Sprays* **6**, 305–329.

Owen, M. J., Gentle, T. M., Orbeck, T. & Williams, D. E. 1988 Dynamic wettability of hydrophobic polymers. In *Polymer Surface Dynamics* (ed. J. D. Andrade). Plenum.

Pasandideh-Fard, M., Chandra, S. & Mostaghimi, J. 2002 A three-dimensional model of droplet impact and solidification. *Intl J. Heat Mass Transfer* **45**, 2229–2242.

Petrov, P. G. & Petrov, J. G. 1992 A combined molecular-hydrodynamic approach to wetting kinetics. *Langmuir* **8**, 1762–1767.

Quéré, D. 2002 Rough ideas on wetting. *Physica* A **313**, 32–46.

Ramé, E., Garoff, S. & Willson, K. R. 2005 Characterizing the microscopic physics near moving contact lines using dynamic contact angle data. *Phys. Rev.* E **70**, 031608(1)–031608(9).

Renardy, Y., Popinet, S., Duchemin, L., Renardy, M., Zaleski, S., Josserand, C., Drumright-Clarke, M. A., Richard, D., Clanet, C. & Quéré, D. 2003 Pyramidal and toroidal water drops after impact on a solid surface. *J. Fluid Mech.* **484**, 69–83.

Richard, D. & Quéré, D. 2000 Bouncing water drops. *Europhys. Lett.* **50**, 769–775.

Rioboo, R., Marengo, M. & Tropea, C. 2002 Time evolution of liquid drop impact onto solid, dry surfaces. *Exps. Fluids* **33**, 112–124.

Schiaffino, S. & Sonin, A. 1997 Molten droplet deposition and solidification at low We numbers. *Phys. Fluids* **9**, 3172–3186.

Schwartz, A. & Tejada, S. B. 1970 Studies of dynamic contact angles on solids. Report. Contract: NAS 3-11522. NASA, Cleveland, OH.

Schwartz, A. M. & Tejada, S. B. 1972 Studies of dynamic contact angles on solids. *J. Colloid Interface Sci.* **38**, 359–375.

Sheng, P. & Zhou, M. 1992 Immiscible-fluid displacement contact line dynamics and the velocity dependent capillary pressure. *Phys. Rev.* A **45**, 5694–5708.

Shibuichi, S., Yamamoto, T., Onda, T. & Tsujii, K. 1998 Super water- and oil-repellent surfaces resulting from fractal structure. *J. Colloid Interface Sci.* **208**, 287–294.

Shikhmurzaev, Y. 1993 The moving contact line on a smooth solid surface. *Intl J. Multiphase Flow* **19**, 589–600.

Wenzel, R. N. 1936 Resistance of solid surfaces to wetting by water. *Indust. Engng Chem.* **28**, 988–995.

Yarin, A. L., Liu, W. & Reneker, H. 2002 Motion of droplets along thin fibers with temperature gradient. *J. Appl. Phys.* **91**, 4751–4760.

https://doi.org/10.1017/S0022112006000231 Published online by Cambridge University Press